Kaunas University of Technology

Faculty of Mathematics and Natural Sciences

Moiré and Superlattice Formation Using Holographic Lithography

Master's Final Degree Project

Gvidas Klyvis

Project author

Prof. Dr. Tomas Tamulevičius

Supervisor

Kaunas, 2022

Kaunas University of Technology

Faculty of Mathematics and Natural Sciences

Moiré and Superlattice Formation using Holographic Lithography

Master's Final Degree Project

6213CX001 Materials physics

Gvidas Klyvis

Project author

Prof. Dr. Tomas Tamulevičius

Supervisor

Assoc. Prof. Dr. Vytautas Stankus

Reviewer

Kaunas, 2022

Kaunas University of Technology
Faculty of Mathematics and Natural Sciences
Gvidas Klyvis

Moiré and Superlattice Formation using Holographic Lithography

Declaration of Academic Integrity

I confirm the following:

1. I have prepared the final degree project independently and honestly without any violations of the copyrights or other rights of others, following the provisions of the Law on Copyrights and Related Rights of the Republic of Lithuania, the Regulations on the Management and Transfer of Intellectual Property of the Kaunas University of Technology (hereinafter – University) and the ethical requirements stipulated by the Code of Academic Ethics of the University;

2. All the data and research results provided in the final degree project are correct and obtained legally; none of the parts of this project are plagiarized from any printed or electronic sources; all the quotations and references provided in the text of the final degree project are indicated in the list of references;

3. I have not paid anyone any monetary funds for the final degree project or the parts thereof unless required by the law;

4. I understand that in the case of any discovery of the fact of dishonesty or violation of any rights of others, the academic penalties will be imposed on me under the procedure applied at the University; I will be expelled from the University and my final degree project can be submitted to the Office of the Ombudsperson for Academic Ethics and Procedures in the examination of a possible violation of academic ethics.

Gvidas Klyvis

Confirmed electronically

Klyvis, Gvidas. Moiré and Superlattices Formation using Holographic Lithography. Master's Final Degree Project / supervisor Prof. Dr. Tomas Tamulevičius; Faculty of Mathematics and Natural Sciences, Kaunas University of Technology.

Study field and area (study field group): Material physics.

Keywords: Moiré, superlattice, holographic lithography.

Kaunas, 2022. Number of pages 48.

Summary

Optical lithography allows to pattern flat surfaces using masks and UV light, but the resolution is limited by the quality of the mask and diffraction of light. One of the ways to pattern sub-wavelength structures without physical masks is holographic lithography. Instead of masks, light fringes are formed by the interference of laser beams. Two beam interference results in a simple sinusoidal pattern, however by adding several of such patterns on top of each other, more complex periodic structures such as Moiré patterns and superlattices can be formed, which can have interesting properties. Lloyd's mirror interferometer was used to produce periodic structures carrying both nanometer and millimeter periodicities on the centimeter scale areas.

Klyvis, Gvidas. Muaro ir supergardelių formavimas naudojant holografinę litografiją. Magistro baigiamasis projektas vadovas prof. dr. Tomas Tamulevičius; Kauno technologijos universitetas, matematikos ir gamtos mokslų fakultetas.

Studijų kryptis ir sritis (studijų krypčių grupė): Medžiagų fizika.

Reikšminiai žodžiai: Muaro gardelės, supergardelės, holografinė litografija.

Kaunas, 2022. Puslapių sk. 48.

Santrauka

Optinė litografija leidžia perkelti struktūras ant kitų medžiagų paviršiaus naudojant kaukes bei UV šviesą. Šios litografijos raišką riboja kaukių kokybė ir šviesos difrakcijos reiškiniai. Viena iš litografijos alternatyvų, kur nereikalingos kaukės, yra holografinė litografija. Šiuo atveju periodinį raštą formuoja lazerio pluoštų interferencijos skirstinys. Dviejų pluoštų interferencijos rezultatas yra sinusinio interferencijos skirtinio periodinė struktūra, tačiau naudojant kartotinę ekspoziciją gaunamos sudėtingesnės struktūros, pvz.: Muaro gardelės bei supergardelės, turinčios įvairių unikalių savybių. Šiame darbe Lloydo veidrodžio interferometras buvo naudojamas struktūrų pasižyminčių tiek milimetriniu tiek nanometriniu periodiškumu formavimui centrimetriniuose plotuose.

Table of Contents

List of Figures

List of Tables

List of abbreviations and terms

Abbreviations:

DNQ – Diazonaphthoquinone;

2D – 2 dimensional;

LSPR – local surface plasmon resonance;

SPP – surface plasmon polariton.

HeCd – Helium Cadmium.

Introduction

According to the Merriam-Webster dictionary [1], the first definition of lithography is printing with a flat surface that has ink repellent and receptive areas. However, that definition is for the printing on paper, while the other definition “the process of producing patterns on semiconductor crystals for use as integrated circuits” is the prominent one considering surface manufacturing technologies [2], and is often accompanied by the method of processing, such as photolithography, electron lithography, ion beam lithography. These methods have many uses, however, nearly everyone has seen the results of at least extreme ultraviolet lithography, as it is to be the prominent technology in the manufacturing of processing units, used in contemporary phones and computers. The feature sizes achievable with the current technology are in the single-digit nanometer range [3], and there are plans to achieve a one-nanometer feature size. However, such machines cost 200 million euros and are very complex to build and operate [4]. Because of that, outside of cutting-edge processor manufacturing, different emerging lithography methods are investigated and employed.

Nowadays there are many different methods to fabricate nanostructures: top-down, namely electron lithography, ion beam lithography, photolithography; bottom-up – annealing after magnetron sputtering, chemical vapor deposition, etc. All of these methods have their own advantages and disadvantages. For example, electron lithography has high precision but is very slow in patterning. Photolithography is a very useful high throughput method, but it requires masks that are expensive to make for each new design. An alternative for photolithography is interference lithography or holographic lithography. This is also a fast and large area method, however, it is limited to periodic structures: one exposure using two laser beams produces a sinusoidal line pattern, however, more complex structures can be made by the superpositions of such a structure with various periods, and at various angles. By exposing twice at various angles, one can produce crystal-like lattice structures [5], however, a more interesting effect occurs, when the exposures differ very slightly, either by a period of the structure, or rotation resulting in additional orders of magnitude larger periodicity. This effect is called Moiré, from the textile with a wavy appearance [6]. These structures have many interesting effects, like high order symmetry, lasing in a Moiré cavity, wide angle perfect absorbers which were analyzed in some studies [7-11].

This work aims to pattern and characterizes Moiré patterns and superlattices using holographic lithography.

Tasks

1. To pattern 2D nanostructures with superlattice amplitude variation over periods larger than 10 µm.
2. Measure fabricated superlattice and nanostructured photoresist contact angle with water dependence on different periods of 200nm and 300nm nanostructures, and 50 µm, 100 µm, 200 µm and 1000 µm superlattices.
3. Provide theoretical accumulated interference field calculations and exploit it for explanation of the experimental periodical patterns imposed in the positive tone photoresist.

1. Literature Review

In this literature review, the basics of photolithography will be briefly reviewed, and then several articles, made in the past few years on the topic of Moiré in photolithography will be summarized.

1.1. Photoresist

Photolithography is a material surface patterning technique based on the use of a photoresist, which is a material that changes its chemical structure in exposure to specific frequencies of light. Photoresists are commercial products and there exist many suppliers, but they can be categorized into two types: positive and negative tone photoresists.

In [12] it is explained that a common type of positive tone photoresists is made from Novalak, a phenol resin, to which a chemical called Diazonaphthoquinone (DNQ) is added. When DNQ is added, the solubility of the mixture in an alkaline medium is much lower than pure Novalak. However, when light with a wavelength within 320-440 nm interacts with the DNQ molecule, the molecule is converted into a carboxylic acid, significantly increasing the solubility (Fig. 1), and also releasing some nitrogen gas, which may cause unwanted bubble formation on the photoresist.

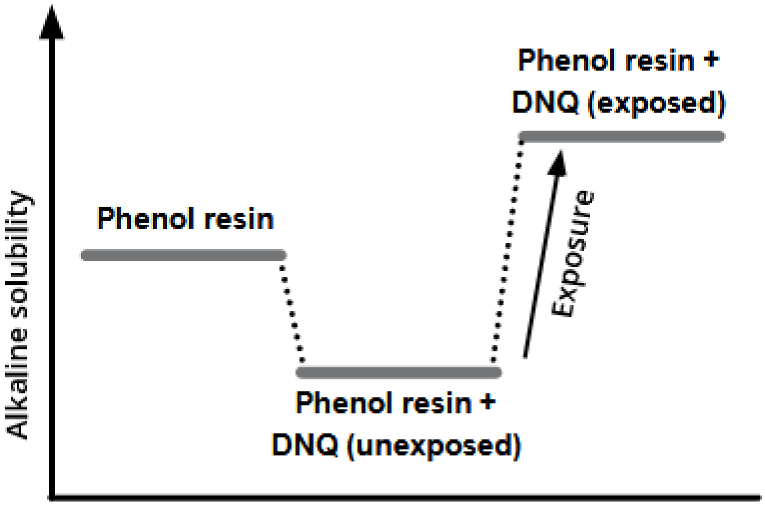

Figure 1. Solubility changes of phenol resin with the addition of DNQ and exposure [12].

In the case of negative tone photoresists, carboxylic acid also forms, but upon heating, it cross-links into longer polymer chains and becomes insoluble. This way, by adding the exposed sample into an alkaline solution for a specific amount of time, using the same exposure pattern, one can obtain either the direct pattern or the inverse pattern, depending on the type of photoresist used. Additionally, there are image reversal photoresists, which work as either positive type, or in the case of heating before adding to an alkaline solution, negative type (Fig. 2) [12].

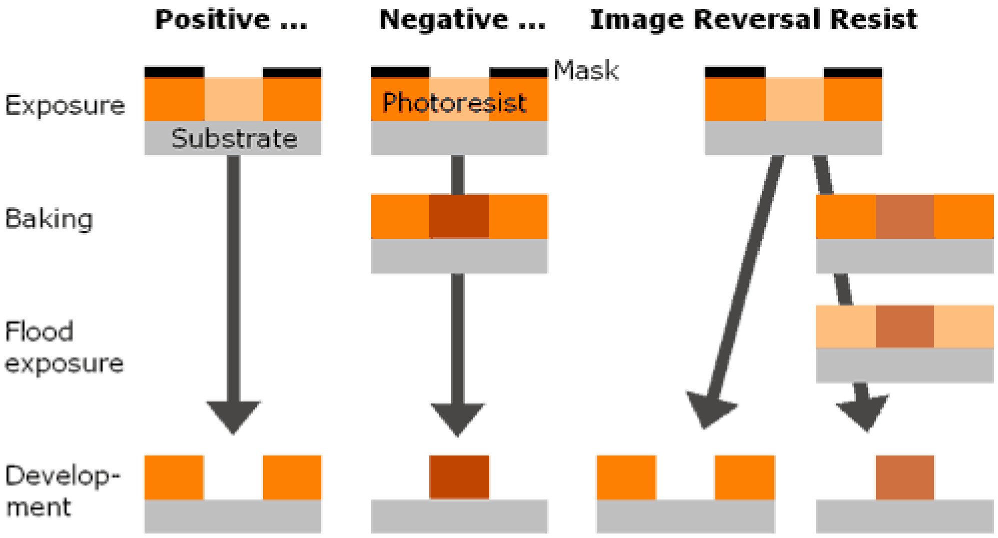

Figure 2. The resulting patterns depending on the photoresist type [12].

In photolithography, depending on the light source used, the fabricated structures are often on the nanometer – micrometer scale. Because of this, the surface of the photoresist in which the structures are made must be completely flat. The technique most commonly chosen to accomplish such a task is called spin coating (Fig. 3) [13].

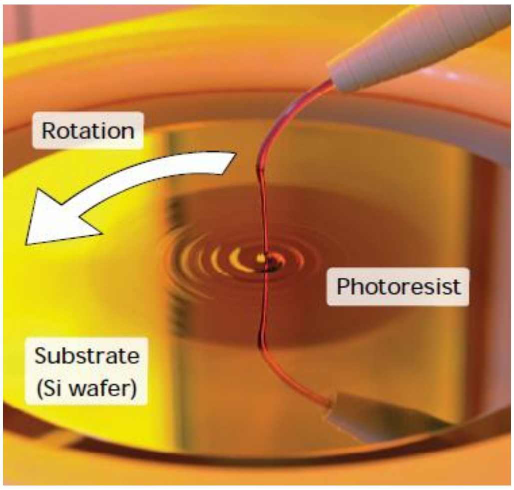

Figure 3. Photoresist application on a silicon wafer by spin coating [13].

During spin coating, a sample that will be coated with a photoresist is placed on a spin coater, and a vacuum is applied to hold the sample in place. Then a drop of a few microliters of photoresist in a liquid solvent is dropped on the center of the sample and the spin coater is turned on to spin at speeds of several thousand rotations per minute. The centrifugal force from spinning causes the photoresist to spread over the surface of the sample and depending on the viscosity of the photoresist and speed of rotation, any excess photoresist runs from the center over the edge and leaves the sample. The high centrifugal forces ensure that the surface is very smooth, without hills or valleys. With a higher viscosity photoresist, the thickness of the photoresist layer on the sample increases. If the sample surface was smooth, before spin coating, then the resulting photoresist layer is smooth and homogeneous. Otherwise, for textured surfaces, the sample is first spun for several hundred rotations per minute for approximately 5 seconds, and the usual spinning spin continues after that since this allows the photoresist to spread more over the textured surface, instead of flying off the sample due to large centrifugal forces [13]. The resulting thickness of the photoresist can be varied by changing the spinning speed. As the speed of rotation is increased, the centrifugal forces increase, and the resulting photoresist thickness is decreased (Fig. 4). When a different thickness is necessary the manufacturers provide the same chemical composition resist of different viscosity (Fig. 4).

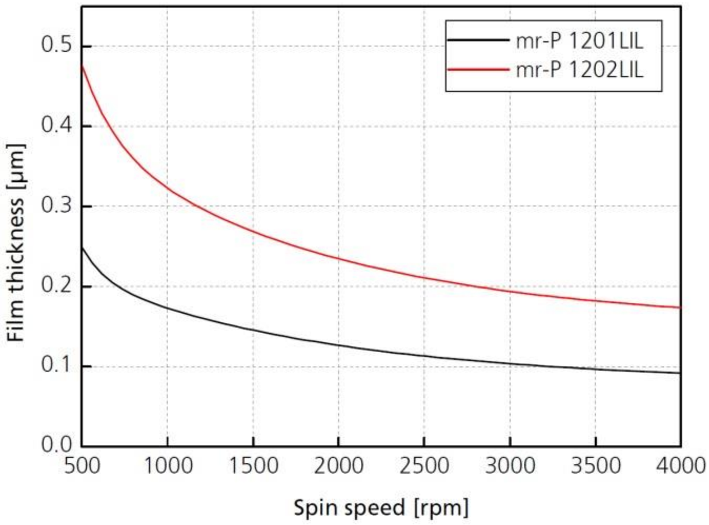

Figure 4. Photoresist film thickness dependence on spin coater spin speed and photoresist type [14].

After spin coating, often a step called prebake, or soft bake is done, to evaporate the solvent from the photoresist. This decreases the number of bubbles of gas formed during the exposition of photoresists [15].

1.1.1. Masked Photolithography

The most commonly used photolithography method for mass production is masked photolithography, in which light from a source passes through a mask and is then incident on the photoresist. The mask is made from a material, which is opaque to the wavelength of light used, but has translucent patterns in the shape of the desired structure. When a parallel light beam impinges on a mask, light passes only the translucent areas and transfers that pattern to the photoresist layer. There are three types of masked photolithography: (i) contact, where the mask is directly placed on the sample, which often leads to the mask degradation; (ii) proximity, where there is a small distance between the sample and mask, but the minimum feature size is larger; however the most common method used is (iii) projection photolithography, in which a system of lenses modifies the light rays that passes through a mask such, that the projection becomes even smaller than the initial mask. This is the method still used in the production of computer chips [16], although the wavelengths used today are in the extreme ultraviolet range, and masks are reflective, not absorbing [17]. The masks for this method are usually created using electron beam lithography, which is a serial exposure method, making the fabrication of masks slow and expensive.

1.1.2. Maskless Photolithography

Instead of using masks to produce patterns, one can also use interference of coherent beams to produce patterns directly. This is utilized in holographic lithography, where a laser beam is split into two and is combined with itself on the photoresist. If one of the beams shines on an object, and the reflection is incident on the photoresist, a hologram is made, which reconstructs the image of the object in the photoresist layer. If no object is in the paths of the laser beams, they will interfere regularly and produce a simple sinusoidal pattern. This is exploited in two-beam lithography, where a beam splitter splits the laser beams, which are reflected on mirrors onto the photoresist (Fig. 5 a). However, the beams do not necessarily have the same optical paths, which means that they are very sensitive to vibrations and airflow, therefore they require specific vibration-absorbing stands, without which the pattern on the sample would have many defects and not produce the expected image. Another holographic photolithography method is Lloyd’s mirror interferometry, which uses a mirror next to the sample, thereby decreasing the optical path, leading to less sensitivity to vibrations and airflow [5]. Principle optical setup layouts of both holographic lithography methods are depicted in Fig. 5.

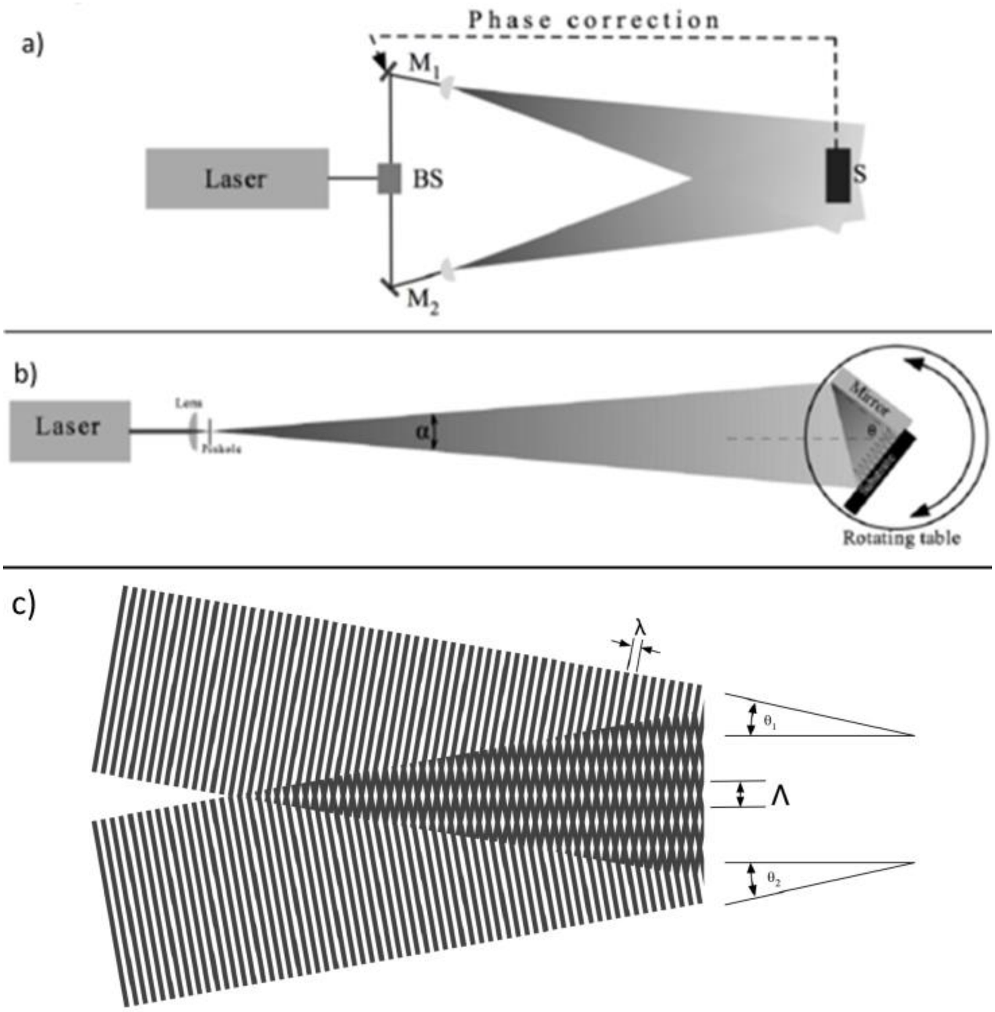

Figure 5. a) Two beam interference lithography. b) Lloyd’s mirror interference lithography. (c) Interference pattern of two beams [5].

The pitch of the interference fringes can be varied by changing the angle between the interfering beams. In Lloyd’s mirror interferometer, when the sample is positioned perpendicular to the mirror, the pitch of the resulting sinusoidal patterns is [5]:

$$d = \frac{\lambda}{2 \cdot \sin\theta}\ , \qquad (1)$$

where d is the period of sinusoidal pattern, λ is the wavelength of laser light, θ is the angle between laser beam and sample surface normal.

In [5] it is mentioned that for the Lloyds' mirror interferometer, the exposure area is limited when the angle is low, according to this equation:

$$EA = Mx \cdot My \cdot \tan\theta \qquad (2)\ [5]$$

When using this equation for 10° the tangent multiplier for the area is only 0.17, while for 47°, it is 1.07.

1.2. Structures Made from Sinusoidal Patterns

While single parallel line structures, and 2-dimensional (2D) crystal structures have been made using holographic lithography for many years, in recent years, more complicated structures that are composed of several exposures with small changes in structure periods, or the same patterns rotated by a small angle have been fabricated and analyzed [7-11].

1.2.1. Single or Double Exposure Structures

Periodic structures have been used for a long time in optics, with the simplest example being linear diffraction gratings, made from a repeating sinusoidal pattern of a specific pitch. According to [18], diffraction gratings are "a collection of reflecting or transmitting elements separated by a distance comparable to the wavelength of light under study". They are used in spectroscopic instruments to spatially separate the different frequencies of light. Double exposure enables the patterning of various 2D crystal lattices, as was shown in [5]. Such 1D and more complex 2D periodic structures were used to originate nearly perfect light absorbers, which were used in sensing hydrogen concentrations in air as depicted in Fig. 6. [19]. In their work, [19] used a Helium-Cadmium (He-Cd) laser, in a Lloyd mirror interferometer setup, to expose a 90nm thick photoresist film, after which they etched the resulting pattern into palladium layer below the photoresist. Their resulting grating had a period of 450nm, and the width of the wires, Fig. 6 (b) was 120nm. The grating had near perfect absorption around 740nm wavelength of light, which changes sufficiently to be detectable at concentrations of hydrogen of 5%.

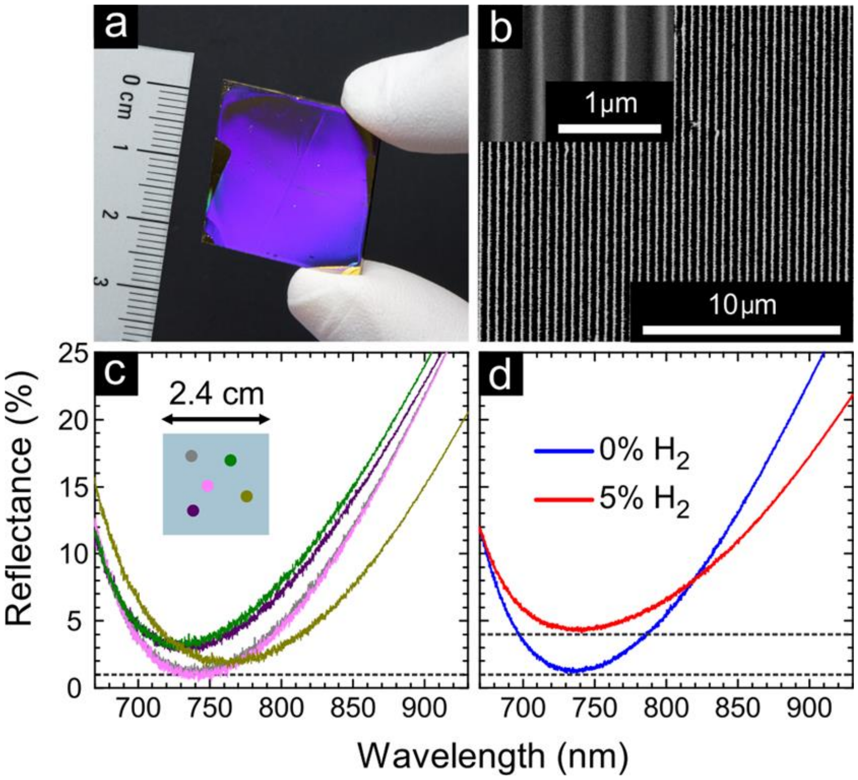

Figure 6. Single exposure holographic lithography made structure with palladium wires: (a) sample, (b) structure of palladium wires, (c) homogeneity over area, (d) reflectance sensitivity to hydrogen. [19]

A gold nano disk array has been used to excite localized surface plasmon resonance (LSPR) for sensing applications in Fig. 7 [20]. There the author used two beam interference lithography, with an argon ion laser, and then after exposure and development, coated the sample with gold and performed lift-off to produce a gold nano disk array, which was used to detect immunoglobin from human blood.

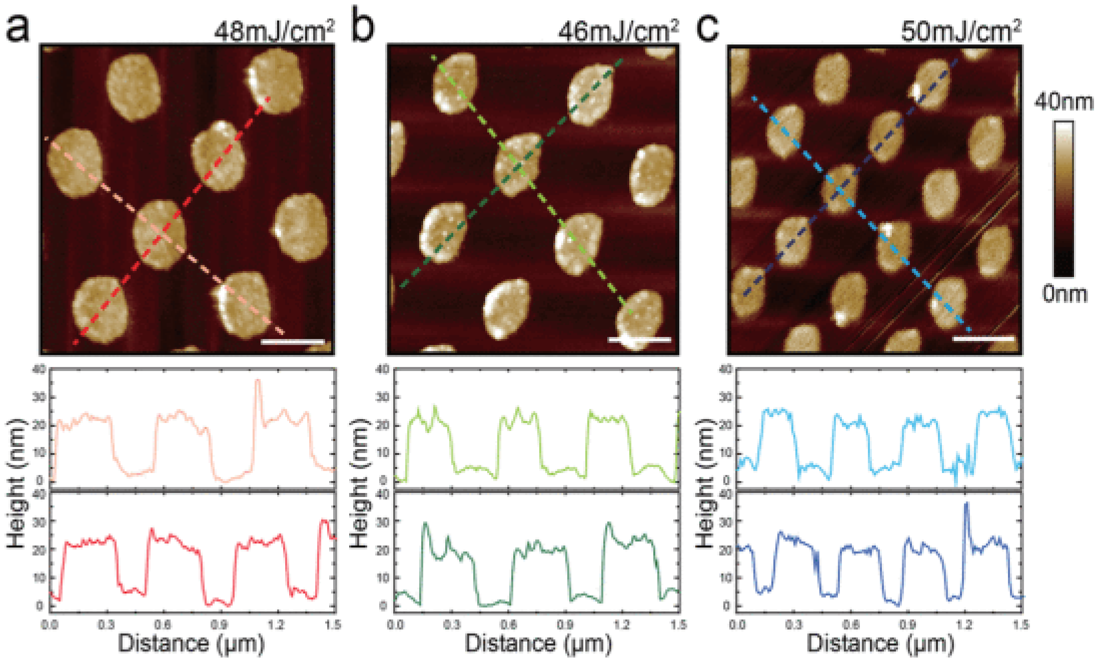

Figure 7. Gold nano disk array used in a LSPR sensor, disk height and size change with exposure energy change [20].

1.2.2. Categorization of Complex Structures

In their study, Russell *et al.* [7] utilized a Lloyd's mirror interferometer to perform multiple exposures on a photoresist coated glass substrate resulting in a range of very different periodic patterns. They classified the structures that could result from these variations into 5 categories: (i) Conventional lattices, (ii) Quasilattices, (iii) Moiré lattices, (iv) Superlattices, and (v) Incommensurate Moiré lattices that are depicted in Fig. 8. Conventional lattices are those, that have clear periodicity, and can be described by lattice vectors (Fig. 8 a). They have long been used in spectroscopic instruments as dispersion elements, to separate the different wavelengths of light. Quasilattices are produced when exposures are done in such a way, that 180° are divided into at least 4 equal parts, and the sample is rotated by this amount after each exposure (Fig. 8 b). These quasilattices do not have translational symmetry but have rotational symmetry and long-range order. Moiré lattices are conventional lattices superimposed onto each other, with a small angle deviation. This causes a small mismatch between periods of the lattices, which causes a variation in the maximum amplitude of the pitches to appear over a much larger pitch than the initial lattices (Fig. 8 c). It has been examined and used in [9], to increase the forbidden bandgap of TM polarized light, as compared to regular square lattices. The sparse modulation pitch can be calculated by this equation [7]:

$$D = \frac{\Lambda}{2\sin\frac{\alpha}{2}}, \quad (2)$$

where D is the sparse modulation pitch resulting from interference from two smaller lattices of dense pitch Λ, α is the mismatch angle between the two lattices.

Superlattices occur when two lattices of different pitches are made in the same direction. The two small pitches are indistinguishable and appear as a single period, however, the overall amplitude of the structure changes continuously over a long period, caused by the mismatch between the two pitches (Fig. 8 d). The smaller the difference between the pitches is, the larger the pitches of the superlattice are. The superlattice pitches can be calculated as:

$$\Lambda_{superlattice} = \frac{\lambda_1}{\lambda_1 - \lambda_2} \cdot \lambda_1, (3)$$

where $\Lambda_{\mathrm{superlattice}}$ is the pitch of the superlattice, λ_1 is the larger of the two pitches, λ_2 is the smaller one.

All lattice types that do not fit into these categories are categorized as incommensurate Moiré (Fig. 8 e) [7]. One use for such structures is photonic bandgap materials, in which the structure of materials is made in such a way, that some wavelengths of light are completely absorbed from all incidence angles.

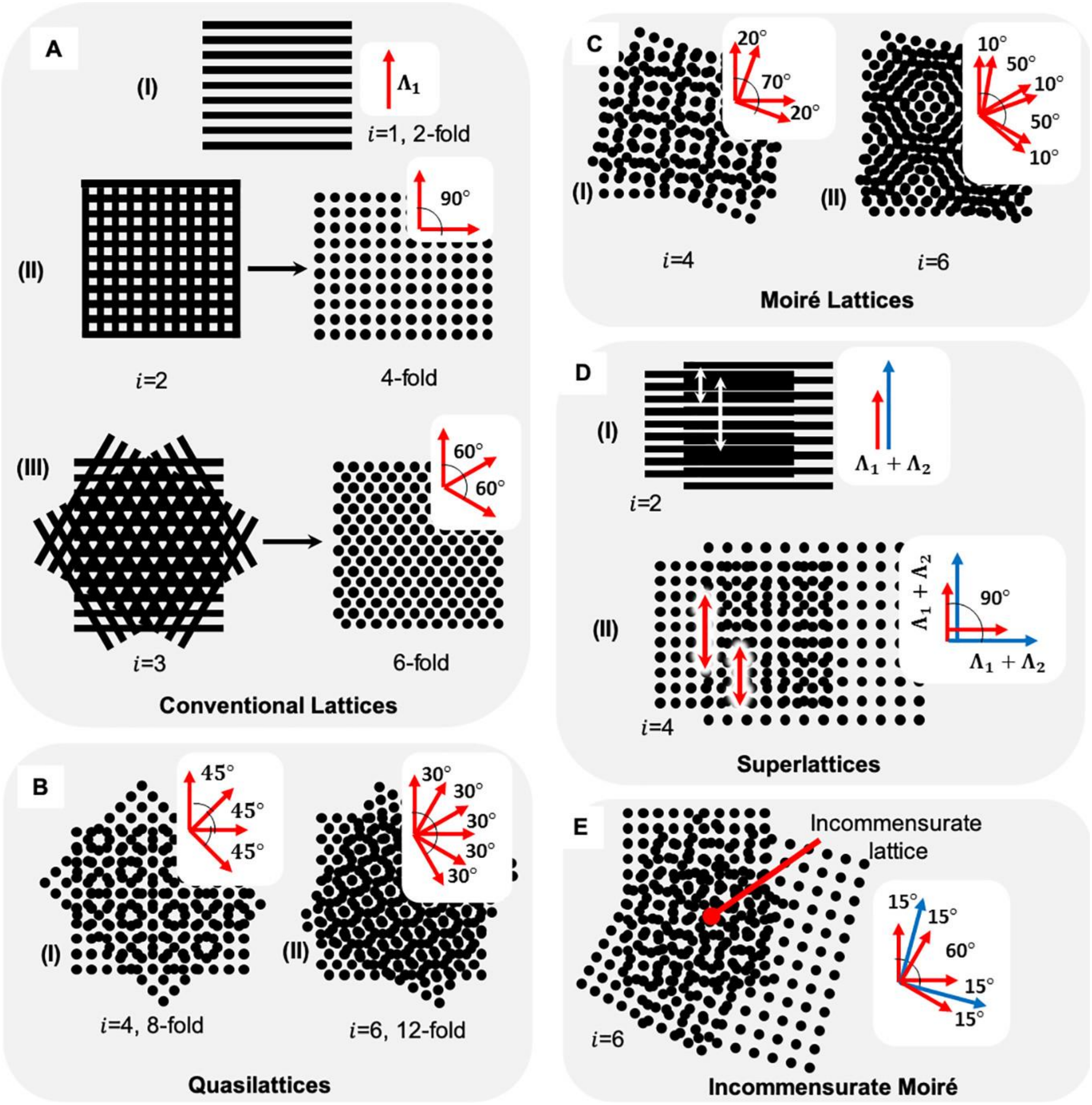

Figure 8. Types of the structure produced by interference lithography. The value of "*i*" is the number of separate exposures necessary to obtain a structure [7].

Russel *et al.* [7] in their study used MATLAB to simulate patterns and then proceeded to fabricate them experimentally. Their samples were cleaned glass substrates. They used Lloyd mirror interferometer in their experiments, and the mirror has been made by depositing a 100 nm silver film on a glass substrate. The laser used in their system was a 405 nm diode laser with a power of 40 mW. The beam went through a spatial filter with a 250 µm pinhole to expand the beam. Their rotation stage had resolution of 0.03. Their fabrication results consisted of rotating the sample by 180^{o} over 3, 4, 5, 6, 7, 8, 9, 10, and 11 exposures, resulting in rotational symmetry in twice the number of exposures, with initial pitches equal to 2 µm; Moiré lattices made from rotating two 7 µm lattices by 5, 10, 20°; superlattices of 23.5µm, and 9.3µm, square lattices, and hexagonal lattices; incommensurate Moiré lattices, made by changing the angle and pitch with each exposure. In addition, they visualized diffraction images from each of these lattices. Such structures have not been widely applied so far but Russel *et al.* [7] in their work speculated that quasilattice structures could have higher quality band gaps, lower coupling losses during light transmission, less sensitivity to anisotropy, and potential applications in beam splitting. They estimated that superlattices could allow great utility in generating and confining slow plasmon modes, which could be used in plasmon lasing applications [21] and could form chiral structures for the detection of chiral molecules.

1.2.2.1. Large Pitch Moiré Patterns

Ushkov *et al.* [11], were trying to overcome the factors limiting Moiré period from being equal to or larger than 1 mm. In their work, the authors utilized the spherical wavefront in a two-beam interferometer and formed Moiré patterns by moving the sample vertically or horizontally after first exposure and then exposing again, or by rotating the sample. They were using a He-Cd laser, and they kept the two beam sources apart at a constant of 69.3cm, and only rotated them to change their angle of incidence, thus causing the grating period to change. They used 1μm, and 300nm grating periods for different Moiré, and the resulting Moiré structures in their work were called "variable depth gratings" since the Moiré period modulates the depth of the nanostructures. They rotated their sample by one to several arcminutes or moved them by several millimeters between exposures. The Fig. 9. Shows how much the sample was moved or rotated by, above the sample, and the resulting Moiré below. Atomic force microscope scanned the surface of sample Fig. 9 (b), in the marked red line, and shows the resulting Moiré height variation in (j). Although the depth modulation was only < 300 nm (Fig. 9), but pitch was up to 15mm, achieved by translating the sample vertically by 5mm, and was clearly visible by the naked eye. They also did a sample with 4 exposures, with two more in perpendicular directions, showing that in such a configuration, different spots on the sample have different topographies. According to the authors, this depth variation can be used to study the depth-dependent effects of metal-dielectric systems, it could also be used to optimize the sensitivity of plasmonic-based sensors, and as diffractive optically variable image devices for anticounterfeiting applications [22].

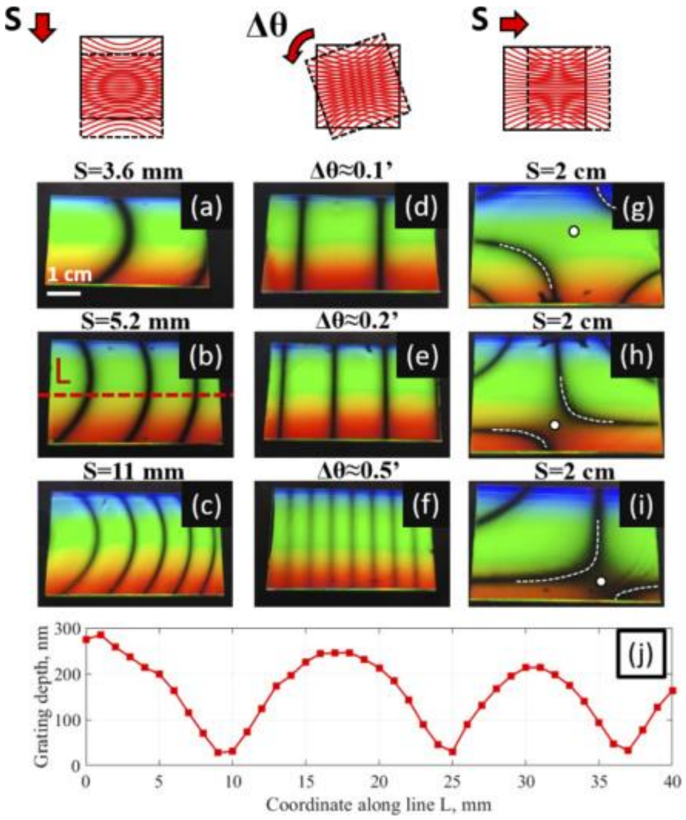

Figure 9. Moiré patterns produced by moving or rotating the sample [11]. (a, b, c) were done by moving the sample vertically from its original position between exposures. (d, e, f) was done by rotating the samples by the indicated degrees between exposures. (g, h, i) were done by translating the sample horizontally by indicated amounts between exposures. In (j) an atomic force microscope data was used to graph the envelope of a Moiré structure.

1.2.2.2. Superlattice Based Laser

The interesting use of superlattices is analyzed by Karademir *et al.* [21], where a superlattice was formed in a photoresist, which was then coated with a thin layer of silver, on top of which a lasing gain medium was deposited. They used a He-Cd ultraviolet continuous wattage laser, by focusing it on a pinhole, and then using the expanded beam on a rotary Lloyd mirror interferometer stage. The superlattice structure formed cavities, where the speed of light was decreased, effectively confining plasmons in the cavity. By pumping light onto the gain medium, the superlattice confined surface plasmon polaritons (SPP) increased the interaction time between SPP and the gain medium. Using the Kretschmann configuration (Fig. 10) to excite surface plasmon resonance, the full width at half maximum linewidth was decreased from 60 nm in gain medium photoluminescence from the dye to 2.7 nm from the surface plasmon resonance lasing. Additionally, they found that by increasing the period of the nanostructure, the resulting lasing wavelength became redshifted, and the full width half maximum increased [21].

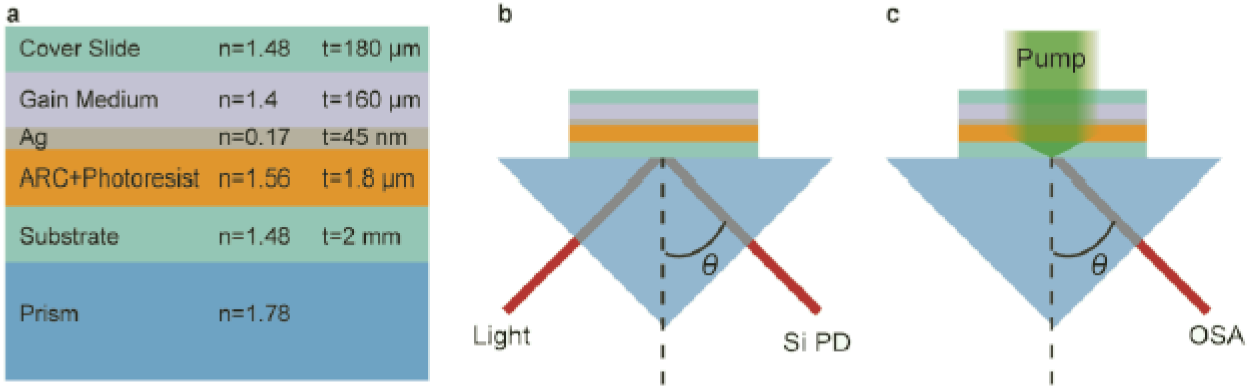

Figure 10. (a) The composition, (b) reflection measurements, and (c) lasing of superlattice laser [21].

1.2.2.3. Moiré Patterns for Increasing Raman Scattering

Nanostructures are often employed in surface-enhanced Raman scattering because they can increase the signal strength up to 10^8 times [23]. However, often the used nanostructures are simple hole or pillar arrays, leaving more complex structures largely unresearched [24]. Seong *et al.* [24] used Lloyds' mirror interferometer to expose the sample twice with perpendicular directions, and on top of that added another exposure of either 60° or 45° degrees. They found that certain areas of complex patterns demonstrated 56.3% higher signal enhancement when compared to conventional hole pattern structures. However, this dependence of enhancement on different areas in the same complex geometry complicates measurements, requiring a sufficient area to be measured to prevent artifacts. Analogously, Mehvar *et al.* [25], used electron-beam lithography to fabricate a double cone structure, in which, instead of a pillars array, each pillar is replaced by two side by side cones. Using this structure, they managed to achieve a signal enhancement of $7.47 \cdot 10^9$.

1.3. Contact angle

The atoms in bulk of a material are surrounded on all sides by similar atoms. However, at the surface, one side of atoms are exposed to a different material than the bulk. The interaction with this different material is weaker than the interaction with bulk, and this can cause there to be higher attraction towards the bulk of the material, instead of the different material, and it can be characterized by surface free energy [26]. This surface energy is most often inferred from a measurement of the contact angle of the surface with different liquids, surrounded by a gas [27]. To solve the equations for surface energy, it is required to use three different liquids with known surface energies [28]. While knowing the surface energy allows some indications of how the material would interact chemically with other materials, simply the contact angle with water by itself is an interesting topic. The lotus effect found in nature is one of such interesting topics, since it is super hydrophobic and has self-cleaning properties, and many papers tried to replicate this effect [29-32]. In these papers, the super hydrophobicity effect is attributed to the hierarchical structure, composed of microstructure and nanostructure, such as the one in Fig. 11, described by Han *et al.* [30]. In their work, the microstructure was formed by femtosecond laser ablation, with laser power of 5 or 10 W, scanning ranges between 50 and 500 mm/s, and microstructure periods of 10, 40, 60, 80, 100, 120 µm. In their work, it is explained that the nanoparticles are caused by the deposition of the low energy plasma left after ablation and are not controlled. Their experiments suggest that microstructures with periods of 40 µm were the most durable and still had superhydrophobic contact angle.

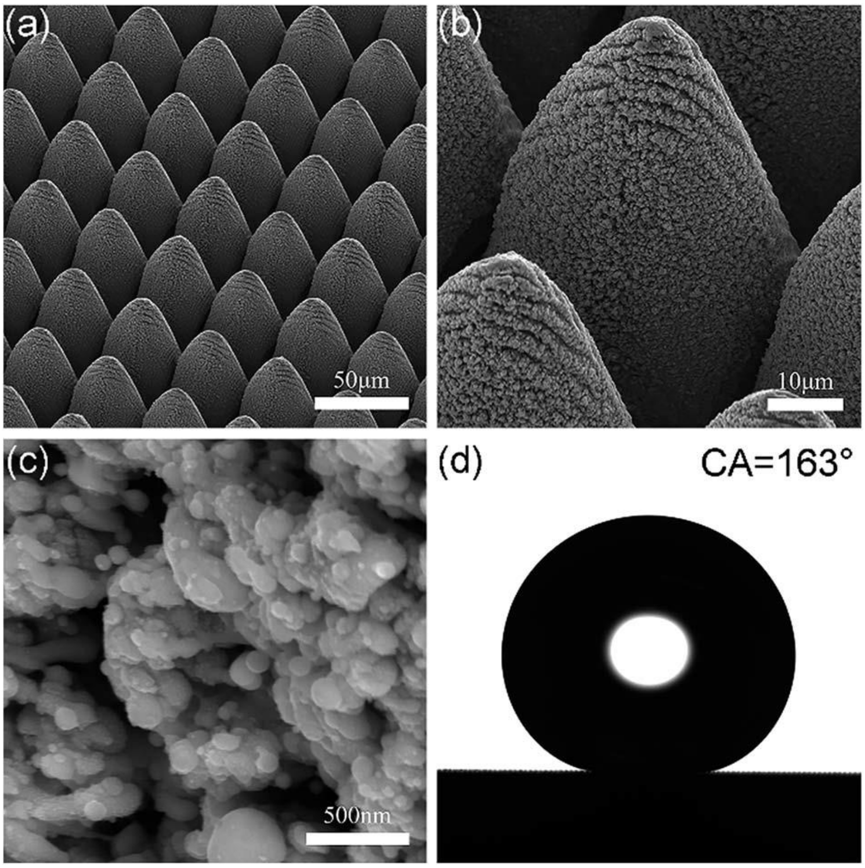

Figure 11. Hierarchical copper structure, formed by 40 μm period microcones (a), and magnification of nanoparticles that cover each of the microcones (b). The superhydrophobic contact angle with 5 μl water drop was shown in (d) [30].

1.4. Justification of topic

In various research papers, hierarchical structures have been made with two beam interferometers, femtosecond lasers and Lloyd’s mirror interferometers. However so far, only a few of the near infinite amount of possible Moiré and superlattice structures have been explored, with growing interest in these structures in recent years. As such, this work will attempt to simulate, fabricate, and measure several superlattice structures, with varying nanostructure periods and superlattice periods.

2. Methods

2.1. Photoresist Deposition

In this work, a positive type of photoresist, ma-P 1201LIL, obtained from Micro resist technology [14] was used, which is originally intended for wavelengths of light between 350 and 450 nm (Fig. 12). Pieces of crystalline silicon wafers were cut to be with sizes of 25 mm x 25 mm. In a chemical laboratory, with the fume hood turned on, the silicon substrates were placed in the middle of a spin coater, and its vacuum was turned on. A small amount of photoresist was taken by a pipette and manually dispensed on the center of the silicon piece, while simultaneously the spin coater was turned on. The rotation speed was set to 3000 rotations per minute, and it continued for 30 seconds, which should leave a photoresist thickness of approximately 100 nm (see Fig. 4), according to the manufacturer's specifications [14]. Because the used spin coater does not have multiple stages option, the optimal initial spinning at 500 rotations per minute for 5 seconds was not done. After the coating, the piece of silicon with photoresist was placed on a piece of filtration paper, until all pieces of silicon were coated. Then they were all added onto a heat plate, which was heated to the specified prebake temperature of 105°C. Prebaking evaporates most of the remainder of the solvent in the coated photoresist, which decreases the formation of nitrogen bubbles during exposure. After 1 minute of soft baking, the samples were added to a Petri dish and moved to the storage drawer to prevent unwanted exposure to the photoresist.

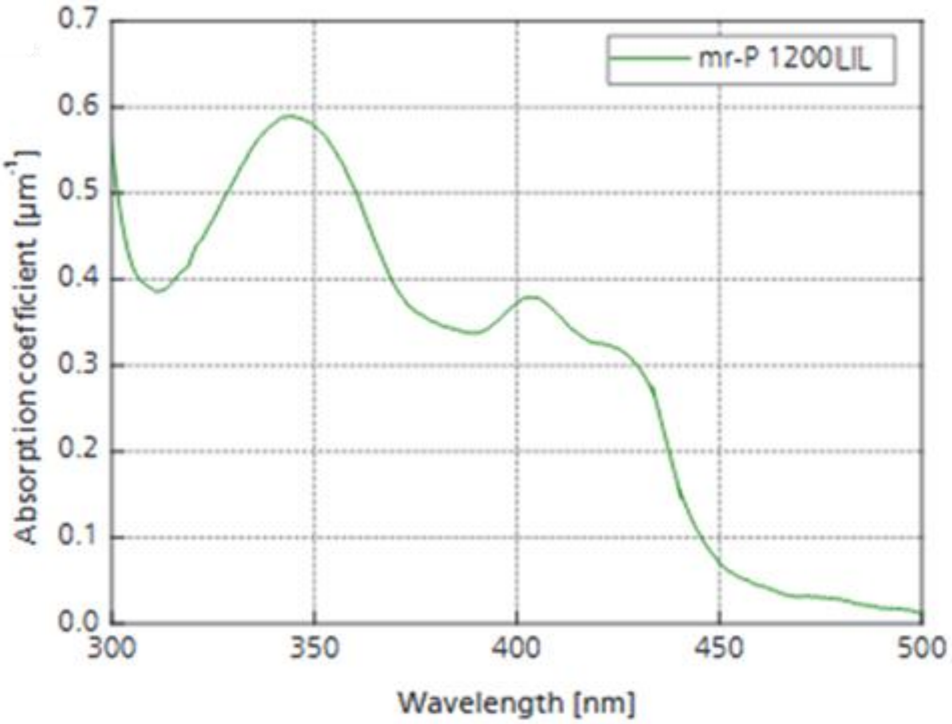

Figure 12. Photoresist series mr-P 1200LIL absorption dependence on light wavelength [14].

2.2. Sample Exposure

2.2.1. Laser System

It is known that only coherent light interferes, therefore it is best to use the same light source. In this work, the light source was a semiconductor laser *L375-015-S* (Crystal laser) Fig. 13 (1) [33], which had a power of 15 mW, and a wavelength of 371 nm. Its manufacturer declared length of coherence is 20 m. The distance from the laser head to the sample holder is 4 m. The beam diameter exiting the laser is 1.1 mm, which is a too-small area for particular experiments, therefore beam expanding optics were used. The laser beam was guided by two laser line dielectric mirrors Fig. 13 (2,3) into a precision spatial filter Fig. 13 (4,5) (*10SF130*, Standa) [34] assembly which is composed of a *U-27X-LC* (Newport) Fig. 13 (4) [35] microscope objective designed for ultraviolet frequencies. The focused beam was filtered with a 15 µm diameter precision *Thorlabs P15D* pinhole Fig. 13(5). The spatial filter helped to clean the laser beam and only the central Gaussian spot portion of the beam was allowed to pass. However, since there is not enough path length for the laser beam to expand sufficiently to cover the sample holder and mirror on the used optical table, a convex lens Fig. 13 (6) was added to expand the beam even more.

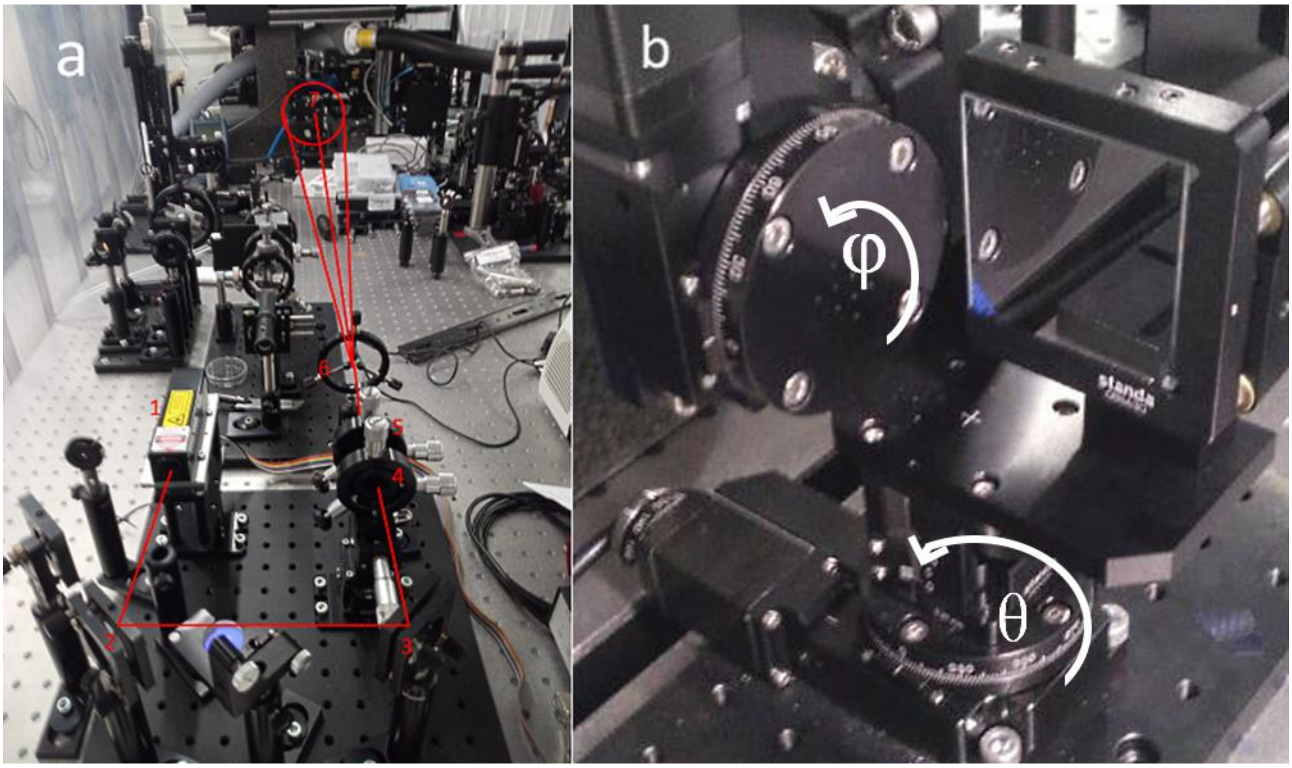

Figure 13. Laser system. (a) (1) laser source, (2), (3) dielectric mirrors, (4) UV lens, (5) 13 µm pinhole, (6) beam expanding lens, (7) sample holder. The beam path is the red line drawn from the laser to the sample holder. (b) sample holder and mirror. The rotation of the angle θ changes nanostructure period, while φ is the tilt angle.

The system works well for expositions, where the pitch of the manufactured sinusoidal pattern is below 300 nm, however, it encounters difficulties when the period is higher than 300 nm. This problem is because in which the reflection of the mirror fails to reach the center of the sample holder when the pattern period is 600 nm but is sufficiently large when the pattern period is 250 nm. For cumulative exposures, automated rotation of the sample in the sample holders' plane was possible for patterns with pitches lower than 300 nm. A 600 nm pattern can be exposed by placing the sample not in the center but closer to the mirror implying some experimental limitations.

The sample holder "*8MR151-Motorized rotation stage*" [36] and laser are controlled by a LabVIEW code. As the laser wavelength was fixed in our experiments the pitch of the fringes was varied by the horizontal rotation of the platform with a sample holder and a mirror. The tilting of the sample holder (see Fig. 13 b φ) has a minimum step of 0.13°. The rotation of sample holder-mirror system (see Fig. 13 b θ) has the minimum step of 0.01° [36]. The exposure duration in seconds is controlled from the program, and it automatically starts and stops after the timer runs out. However, since the laser beam is unstable for the first 30 seconds after turning it on, the timer is set to 30 seconds higher than the calculated time for a chosen energy amount, and a piece of white paper is placed between the spatial filter and expanding lens. After the first 30 seconds passed with the laser being on, the white paper is removed manually, and then the laser exposes the sample only with a stable beam. After the first exposure, the software rotates the sample or the sample stage, and another exposure is done. When all exposures are done, the sample manually is placed in ma-D 374/S developer (Micro resist technology) for 10 seconds, while it is continuously stirred. Afterward, the sample is stirred in deionized type 2 water for several seconds and dried blowing with nitrogen gas and keeping the sample perpendicular to the gun, on the sample center until no liquid is visible on the sample.

2.3. Sample Fabrication Parameters

The experimental conditions of the samples investigated in this work are summarized in Table 1. Angle θ is the angle between the direct laser beam and reflected laser beam, Fig. 5 (b). It is controlled by the rotation stage at Fig. 13 (b), bottom, where the angles are marked on the equipment. The sample can also be tilted in place by angle φ, by the rotation stage Fig. 5 (b) top left, which also has angles marked on it. The main parameter of exposures was exposure energy, which is laser emitted power times duration of exposure over a cm^2 area, and angles of rotation θ which determine nanostructure period, and tilt angle φ. Also, the temperature and relative humidity were monitored. Not all results were included in the results, therefore important samples in Table 1 are indicated in grey shading.

Table 1. Experimental exposition parameters

No.	Power, μW	Duration, s	Pitch, nm	Energy, mJ	Angle$_p$, θ	Angle$_r$, φ	H, %	T, °C	Comment
F19	112.1	268	599.97	30.0	18.01	0	43	19.4	Developed a few seconds too long.
F20	112.1	268	599.97	30.0	18.01	0	43	19.4	Mostly without comets.
F21	112.1	268	599.97	30.0	18.01	0	43	19.4	Side without comets. Not cooled down after prebake.
F22	112.1	268	599.97	30.0	18.01	0	43	19.4	Half without comets. Not cooled down after prebake.
F23	112.1	268	599.97	30.0	18.01	0	43	19.4	Heated for 6min after exposure. Developed for 60 seconds. Small area without comets.
F24.1A	128.3	59	299.96	7.5	38.20	0	44	19.4	No photoresist remained after developing for 10 seconds.
F24.1B	128.3	59	295.50	7.5	38.88	0	44	19.4	
F24.2A	128.3	59	299.96	7.5	38.20	90	44	19.4	
F24.2B	128.3	59	295.50	7.5	38.88	90	44	19.4	
F25.1A	128.3	40	299.96	5.1	38.20	0	44	19.4	Only a small corner has photoresist left.
F25.1B	128.3	40	295.50	5.1	38.88	0	44	19.4	
F25.2A	128.3	40	299.96	5.1	38.20	90	44	19.4	
F25.2B	128.3	40	295.50	5.1	38.88	90	44	19.4	
F26.1A	128.3	35	299.96	4.5	38.20	0	44	19.4	
F26.1B	128.3	35	298.20	4.5	38.47	0	44	19.4	
F26.2A	128.3	35	299.96	4.5	38.20	90	44	19.4	
F26.2B	128.3	35	298.20	4.5	38.47	90	44	19.4	

F27.1A	134.0	35	299.96	4.5	38.20	0	37	20.1	50µm Moiré. Contact angle with water 36.2º.
F27.1B	134.0	35	298.20	4.5	38.47	0	37	20.1	
F27.2A	134.0	35	299.96	4.5	38.20	0	37	20.1	100µm Moiré. Contact angle 39.8º. Each Moiré on sample F27 was done on another corner, without affecting each other.
F27.2B	134.0	35	299.10	4.5	38.33	0	37	20.1	
F27.3A	134.0	35	299.96	4.5	38.20	0	37	20.1	200µm Moiré. Contact angle 38.2º.
F27.3B	134.0	35	299.55	4.5	38.26	0	37	20.1	
F27.4A	134.0	35	299.96	4.5	38.20	0	37	20.1	1000µm Moiré. Contact angle 36.2º.
F27.4B	134.0	35	299.91	4.5	38.21	0	37	20.1	
F28	134.0	223	599.97	30	18.01	0	38	20.1	
F29	134.0	50	-	-	-	-	38	20.1	
F30	-	-	-	-	-	-	38	20.1	
F31.1A	122.5	41	299.96	5.0	38.19	0	30	20.7	
F31.1B	122.5	41	291.02	5.0	39.60	0	30	20.7	
F31.2A	122.5	41	299.96	5.0	38.19	90	30	20.7	
F31.2B	122.5	41	291.02	5.0	39.60	90	30	20.7	
F32.1A	122.5	61	299.96	7.5	38.19	0	30	20.7	
F32.1B	122.5	61	291.02	7.5	39.60	0	30	20.7	
F32.2A	122.5	61	299.96	7.5	38.19	90	30	20.7	
F32.2B	122.5	61	291.02	7.5	39.60	90	30	20.7	
F33.1A	115.4	260	200.00	30.0	68.05	0	30	20.7	No photoresist was left after developing.
F33.1B	115.4	260	196.00	30.0	71.16	0	30	20.7	
F33.2A	115.4	260	200.00	30.0	68.05	90	30	20.7	
F33.2B	115.4	260	196.00	30.0	71.16	90	30	20.7	
F34.1A	115.4	173	200.00	20.0	68.05	0	30	20.7	No photoresist was left after developing.
F34.1B	115.4	173	196.00	20.0	71.16	0	30	20.7	
F34.2A	115.4	173	200.00	20.0	68.05	90	30	20.7	
F34.2B	115.4	173	196.00	20.0	71.16	90	30	20.7	
F35.1A	105.4	95	200.00	10.0	68.05	0	30	20.7	
F35.1B	105.4	95	196.00	10.0	71.16	0	30	20.7	
F35.2A	105.4	95	200.00	10.0	68.05	90	30	20.7	
F35.2B	105.4	95	196.00	10.0	71.16	90	30	20.7	
F36.1A	135.6	110	200.00	15.0	68.05	0	11	19.4	Uneven development.
F36.1B	135.6	110	196.00	15.0	71.16	0	11	19.4	
F36.2A	135.6	110	200.00	15.0	68.05	90	11	19.4	
F36.2B	135.6	110	196.00	15.0	71.16	90	11	19.4	
F37.1A	135.6	110	200.00	15.0	68.05	0	11	19.4	Slightly too much exposure or development.
F37.1B	135.6	110	196.00	15.0	71.16	0	11	19.4	
F37.2A	135.6	110	200.00	15.0	68.05	90	11	19.4	
F37.2B	135.6	110	196.00	15.0	71.16	90	11	19.4	
F38.1A	134.2	60	599.97	8.0	18.01	0	27	20.4	Uneven development. A third of the sample shows clear diffraction from 600nm, grating, while another third shows from 250nm. Developed for 1min. Still largely undeveloped.
F38.1B	134.2	60	599.80	8.0	18.02	0	27	20.4	
F38.2A	134.2	60	250.01	8.0	47.90	0	27	20.4	
F38.2B	134.2	60	249.97	8.0	47.91	0	27	20.4	
F39.1	117.7	85	599.97	10.0	18.01	0	-	-	As expected, using the optical stand to rotate the sample vertically, leaves nearly no
F39.2	117.7	85	599.97	10.0	18.01	60	-	-	
F39.3	117.7	85	599.97	10.0	18.01	-60	-	-	

									area where all three structures overlap.
F40.1	117.7	85	250.01	10.0	47.90	0	-	-	250nm structures also do not work, since the laser beam does not cover enough area.
F40.2	117.7	85	250.01	10.0	47.90	60	-	-	
F40.3	117.7	85	250.01	10.0	47.90	-60	-	-	
F41.1A	21.4	234	250.01	5.0	47.90	0	24	19.3	By adding the optical lens, the UV laser beam was expanded and now covers sufficient area to work with 250nm. The 1mm Moiré pattern is visible with the naked eye.
F41.1B	21.4	234	249.97	5.0	47.91	0	24	19.3	
F41.2A	21.4	234	250.01	5.0	47.90	60	24	19.3	
F41.2B	21.4	234	249.97	5.0	47.91	60	24	19.3	
F41.3A	21.4	234	250.01	5.0	47.90	-60	24	19.3	
F41.3B	21.4	234	249.97	5.0	47.91	-60	24	19.3	
F42.1A	21.4	117	250.01	2.5	47.90	0	24	19.3	50µm Moiré structures are not visible with the naked eye, and the optical microscope did not show anything. Perhaps too low energy for each exposure.
F42.1B	21.4	117	248.75	2.5	48.22	0	24	19.3	
F42.2A	21.4	117	250.01	2.5	47.90	30	24	19.3	
F42.2B	21.4	117	248.75	2.5	48.22	30	24	19.3	
F42.3A	21.4	117	250.01	2.5	47.90	60	24	19.3	
F42.3B	21.4	117	248.75	2.5	48.22	60	24	19.3	
F42.4A	21.4	117	250.01	2.5	47.90	90	24	19.3	
F42.4B	21.4	117	248.75	2.5	48.22	90	24	19.3	
F42.5A	21.4	117	250.01	2.5	47.90	-30	24	19.3	
F42.5B	21.4	117	248.75	2.5	48.22	-30	24	19.3	
F42.6A	21.4	117	250.01	2.5	47.90	-60	24	19.3	
F42.6B	21.4	117	248.75	2.5	48.22	-60	24	19.3	
F43.1A	21.4	234	250.01	5.0	47.90	0	24	19.3	After developer has been poured for 3 hours and several samples were developed it was not enough to develop this sample. A fresh batch of developer needed 30 seconds to sufficiently develop this sample.
F43.1B	21.4	234	249.97	5.0	47.91	0	24	19.3	
F43.2A	21.4	187	250.01	4.0	47.90	60	24	19.3	
F43.2B	21.4	187	249.97	4.0	47.91	60	24	19.3	
F43.3A	21.4	140	250.01	3.0	47.90	-60	24	19.3	
F43.3B	21.4	140	249.97	3.0	47.91	-60	24	19.3	
F44.1A	21.4	234	250.01	5.0	47.90	0	24	19.3	
F44.1B	21.4	234	249.97	5.0	47.91	0	24	19.3	
F44.2A	21.4	234	250.01	5.0	47.90	60	24	19.3	
F44.2B	21.4	234	249.97	5.0	47.91	60	24	19.3	
F44.3A	21.4	234	250.01	5.0	47.90	-60	24	19.3	
F44.3B	21.4	234	249.97	5.0	47.91	-60	24	19.3	
F45.1A	20.8	721	999.10	15.0	10.70	0	-	-	
F45.1B	20.8	721	998.18	15.0	10.71	0	-	-	
F46.1A	20.8	721	500.16	15.0	21.77	0	-	-	
F46.1B	20.8	721	499.94	15.0	21.78	0	-	-	
F47.1A	20.8	721	249.97	15.0	47.91	0	-	-	
F47.1B	20.8	721	249.93	15.0	41.92	0	-	-	
F48.1A	20.8	721	200.00	15.0	68.05	0	-	-	
F48.1B	20.8	721	199.96	15.0	68.08	0	-	-	
F49.1B	20.8	721	200.00	30.0	68.05	0	-	-	
F49.1B	20.8	721	199.96	30.0	68.08	0	-	-	
G1.A	20.8	721	599.97	15.0	18.01	0	-	-	
G1.B	20.8	721	592.66	10.0	18.24	0	-	-	
G2.1A	19.9	251	599.97	5.0	18.00	90	-	-	
G2.1B	19.9	251	592.66	5.0	18.24	0	-	-	
G2.1C	19.9	251	585.53	5.0	18.47	90	-	-	
G2.2A	19.9	251	599.97	5.0	18.00	0	-	-	

G2.2B	19.9	251	592.66	5.0	18.24	90	-	-	
G2.2C	19.9	251	585.53	5.0	18.47	0	-	-	
G3.1A	19.9	327	250.01	6.5	47.90	0	-	-	The reason that G3.C has 1/3 the energy is because that makes the Moiré structures higher contrast in simulation. If G3.C has 3x the energy, Moiré is nearly gone. G3.C is added because it adds spheres on top of intersections. And it makes the structure squarer.
G3.1B	19.9	327	243.75	6.5	49.56	0	-	-	
G3.1C	19.9	111	237.49	2.2	51.36	0	-	-	
G3.2A	19.9	327	250.01	6.5	47.90	90	-	-	
G3.2B	19.9	327	243.75	6.5	49.56	90	-	-	
G3.2C	19.9	111	237.49	2.2	51.36	90	-	-	
G4.1A	22.0	150	599.97	3.3	18.01	0	47	18.1	
G4.1B	22.0	150	592.66	3.3	18.24	0	47	18.1	
G4.2A	22.0	150	599.97	3.3	18.01	60	47	18.1	
G4.2B	22.0	150	592.66	3.3	18.24	60	47	18.1	
G4.3A	22.0	150	599.97	3.3	18.01	-60	47	18.1	
G4.3B	22.0	150	592.66	3.3	18.24	-60	47	18.1	
G5.1A	22.0	150	599.97	3.3	18.01	0	47	18.1	
G5.1B	22.0	150	592.66	3.3	18.24	0	47	18.1	
G5.1C	22.0	150	585.53	3.3	18.47	0	47	18.1	
G5.2A	22.0	150	599.97	3.3	18.01	60	47	18.1	
G5.2B	22.0	150	592.66	3.3	18.24	60	47	18.1	
G5.2C	22.0	150	585.53	3.3	18.47	60	47	18.1	
G5.3A	22.0	150	599.97	3.3	18.01	-60	47	18.1	
G5.3B	22.0	150	592.66	3.3	18.24	-60	47	18.1	
G5.3C	22.0	150	585.53	3.3	18.47	-60	47	18.1	
G6.1A	20.8	721	599.97	15.0	18.01	0	26	18.4	Minimal vertical rotation value.
G6.1B	20.8	721	599.97	15.0	18.01	0.13	26	18.4	
G7.1A	20.8	721	599.97	15.0	18.01	0	26	18.4	
G7.1B	20.8	721	596.45	15.0	18.12	0	26	18.4	
G7.2A	20.8	721	599.97	15.0	18.01	0	26	18.4	
G7.2B	20.8	721	598.36	15.0	18.06	0	26	18.4	
G7.3A	20.8	721	599.97	15.0	18.01	0	26	18.4	
G7.3B	20.8	721	596.45	15.0	18.12	0	26	18.4	
G7.4A	20.8	721	599.97	15.0	18.01	0	26	18.4	
G7.4B	20.8	721	592.66	15.0	18.24	0	26	18.4	
G8.1A	20.8	154	250.01	3.2	47.90	0	34	18.4	No photoresist remained after development. Total energy 32meJ is too much.
G8.1B	20.8	154	249.97	3.2	47.91	0	34	18.4	
G8.2A	20.8	154	250.01	3.2	47.90	0	34	18.4	
G8.2B	20.8	154	249.97	3.2	47.91	0	34	18.4	
G8.3A	20.8	154	250.01	3.2	47.90	0	34	18.4	
G8.3B	20.8	154	249.97	3.2	47.91	0	34	18.4	
G8.4A	20.8	154	250.01	3.2	47.90	0	34	18.4	
G8.4B	20.8	154	249.97	3.2	47.91	0	34	18.4	
G8.5A	20.8	154	250.01	3.2	47.90	0	34	18.4	
G8.5B	20.8	154	249.97	3.2	47.91	0	34	18.4	
G9.1A	20.8	139	250.01	2.9	47.90	0	34	18.4	
G9.1B	20.8	139	249.97	2.9	47.91	0	34	18.4	
G9.2A	20.8	139	250.01	2.9	47.90	0	34	18.4	
G9.2B	20.8	139	249.97	2.9	47.91	0	34	18.4	
G9.3A	20.8	139	250.01	2.9	47.90	0	34	18.4	
G9.3B	20.8	139	249.97	2.9	47.91	0	34	18.4	
G9.4A	20.8	139	250.01	2.9	47.90	0	34	18.4	

G9.4B	20.8	139	249.97	2.9	47.91	0	34	18.4	
G9.5A	20.8	139	250.01	2.9	47.90	0	34	18.4	
G9.5B	20.8	139	249.97	2.9	47.91	0	34	18.4	

2.4. Pattern Simulation Using MATLAB Software

The resulting structures from multiple exposures are superpositions of each exposure with a specific structure pitch, and angle. The simulation of accumulated interference was simulated using MATLAB software. The written code used a portion of the original code from the appendixes in [7], in the form of the function "rotational_symmetry", and "expose". The MATLAB code creates a matrix of chosen size, with chosen value for distance between points in nanometers. The code calculates the total intensity resulting from all exposures, subtracts it from the sum of maximum exposures multiplied by their intensities, and divides the result by the number of exposures multiplied by their intensities. The result is a value from 0 to 1, which shows how much photoresist is left at that point, with 0 being no photoresist, and 1 being unexposed photoresist. The calculation occurs one point at a time, until the entire matrix is calculated. The resulting matrix of values is drawn as a 3D surface by the function "surf". Labels are then added to the figure, and a colormap for height value is added. The code allows the simulation for any number of exposures, with intensity, pitch, and rotation that are variable between each exposure. Additionally, the spatial resolution and simulated area size are easily changeable. The code automatically converts from an image of superposition of intensities to the structure left on photoresist, by subtracting the intensity image from photoresist height. The resulting simulation image shows, the remaining photoresist thickness after developing.

Table 2. MATLAB code for simulation of multiple exposures of interference lithography.

```
clear all;
xmax = 60*10^3;      % length in x axis
ymax = 45*10^3;      % length in y axis
dx = 93;            % Distance between 2 points in the graph in 
nanometers
nx = floor(xmax/dx)*2;% number of points on x axis
ny = floor(ymax/dx)*2;% number of points on y axis

x_space = linspace(-xmax,xmax,nx);   % Setting up array of x axis 
values
y_space = linspace(-ymax,ymax,ny);   % Setting up array of y axis 
values
u = zeros(nx,ny);                    % Creating an empty array to store 
values
for x=1:nx
    for y=1:ny
        tx = (x - (nx/2))*dx;
        ty = (y - (ny/2))*dx;
        temp = rotation_symmetry(tx,ty,600,[0 90],[1 1])
+rotation_symmetry(tx,ty,592.8,[0 90],[1 1])
+rotation_symmetry(tx,ty,585.6,[0 90],[1 1]);
        u(x,y) =  (6 -(temp))/6;
    end
end
f = figure;
[X,Y] = meshgrid(x_space,y_space);
```

```
image = surf(X,Y,u','edgecolor','none');     % This function plots the
graph of remaining photoresist thickness
view(0,90);                     % This part sets the initial angle to be top
down
xlabel('x, nm');
ylabel('y, nm');
colorbar;                       % This adds a bar in which color corresponds to
remaining photoresist thickness
colormap(jet(256));
ax = gca;
ax.XAxis.Exponent = 3;  % This part makes it so that the scale on axis
would be in thousands of nanometers = micrometers
ax.YAxis.Exponent = 3;
set(gca,'FontSize',20)
```

Table 3. MATLAB function for a single exposition of two interfering beams. A modified version of the code used in [7].

```
function exposition = expose(x,y,d,teta)
    exposition = ( (sin( (-x*sin((pi/180)*teta)+y*cos((pi/180)*teta))
*pi/d))^2  );
end
```

Table 4. MATLAB function for exposing a sample at several different tilt angles, and with different amounts of exposure energies. A modified version of the code from [7].

```
function result = rotation_symmetry(x,y,d,teta,pow)
    t_result = 0;
    n = length(teta);
    for i=1:n
        angle = teta(i);
        power = pow(i);
        exposition1      =      (      (sin((      -x*sin((pi/180)*angle)
+y*cos((pi/180)*angle)) *pi/d))^2  ) *power;
        t_result = t_result + exposition1  ;
    end
    result = t_result;

end
```

2.5. Optical microscope

The analysis of fabricated structures was done with an optical microscope, Fig. 14 [37]. The optical microscope has an ocular which has magnification of 10x. It also has a selection of objectives with magnifications of 5x, 10x, 20x, 50x, 100x. The images were done in air, therefore the limit of resolution by diffraction in such a case would be 400 to 700 nm [38]. While low contrast, 600 nm structures are visible with this microscope, but anything below 400 nm is undetectable. The microscope has a camera attached to its top, that can be rotated, and transmits real time image to a computer, that the microscope is connected to. This allows images to be taken and modified in computer software.

Figure 14. Optical microscope image [37].

2.6. Image analysis software ImageJ

Optical microscope images were done with a known size object, which allows to calibrate other images according to known sizes. For such a task, a fork of *ImageJ2* software, *Fiji* was used to analyze the images [39]. *Fiji* software has basic line and figure selection and drawing tools, while most of its functions are for image manipulation, such as image contrast enhancement, conversion to binary, Fast Fourier Transformation, etc. The function important for this work is its ability to easily select a distance, and set its size, and then use the set scale for a different image. Using this, a millimeter scale, with micrometer values was used to set scale for 1500x magnification optical microscope image, and the scale was reused for each image made with 1500x magnification. An image of the software and an analyzed image is shown in Fig. 15. All the functions are contained in the ribbon in the top part of the image. This image already has a scale set, and red ellipses indicate a line on the bottom, and its distance in the top. While the initial MATLAB simulation images were saved in a matrix of 1876 by 1341 points, Fig. 15, images from optical microscope were saved in a matrix of 1296 by 986 points, therefore the simulation images had to be resized, to be closer in size to optical microscope images.

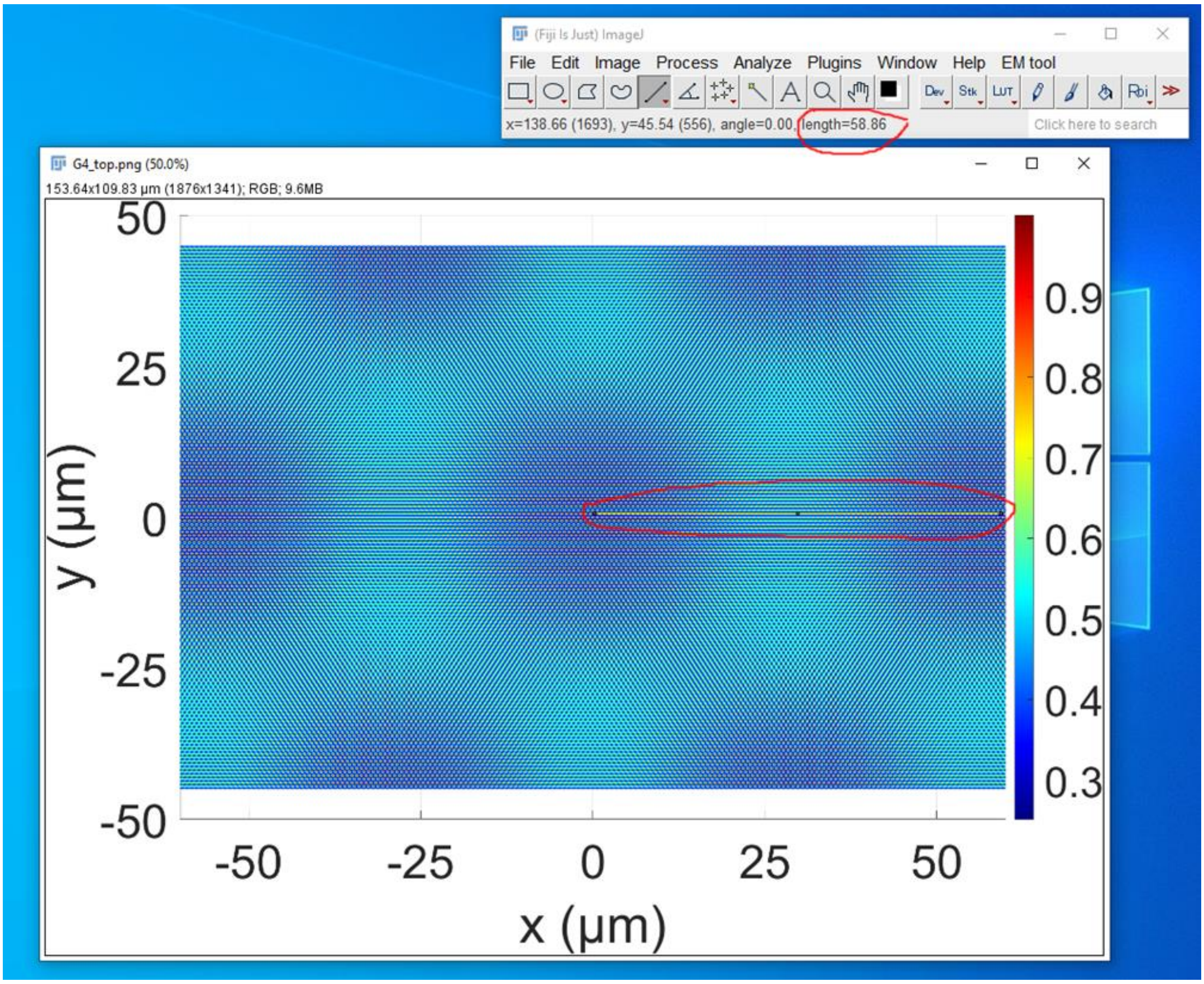

x=138.66 (1693), y=45.54 (556), angle=0.00, length=58.86

153.64x109.83 µm (1876x1341); RGB; 9.6MB

Figure 15. Fiji software

2.7. Contact angle measurement

Contact angle measurements were done with *Kruss DSA25*, contact angle measurer [40]. It has automatic drop dispenser with selectable volume and allows taking images and recordings of the sample with liquid drop. Its storage is filled with type 2 deionized water, which is used to dispense the drops. The accuracy of angle measurement is 0.1°, and the maximum size of the sample is 32 cm by 16.5 cm. The equipment is controlled by software via a computer. In the software, the type of liquid drop shape fitting can be selected from methods such as Ellipse, Young’s, etc. Image of the instrument is shown in Fig. 16. The process of measurement was such: a set amount of size for the droplet of water was selected, and while the syringe with water was far above the sample, a drop was made. Initially after the instrument was not used, the size of droplet of liquid is inaccurate, therefore several times the liquid is dispensed, until a droplet forms, and it is placed on a place in the sample, where it will not disturb the measurements. Then the size of droplets formed becomes accurate, and a droplet of desired size is made. Then the sample stage is slowly brought up, until the sample touches the droplet, and the droplet attaches itself to the sample. Since it is still connected to the syringe, the sample stage is slowly lowered, until the syringe no longer touches the droplet. Then a baseline is set in the software, which shows where the surface of the sample is, where the drop touches. Then a drop of water shape fitting method is selected, and a measurement is made, and is saved as a point in an excel table. At this point, an image of the sample can be made. After the measurement, the sample stage is lowered, and another sample is placed there, and the measurement is repeated.

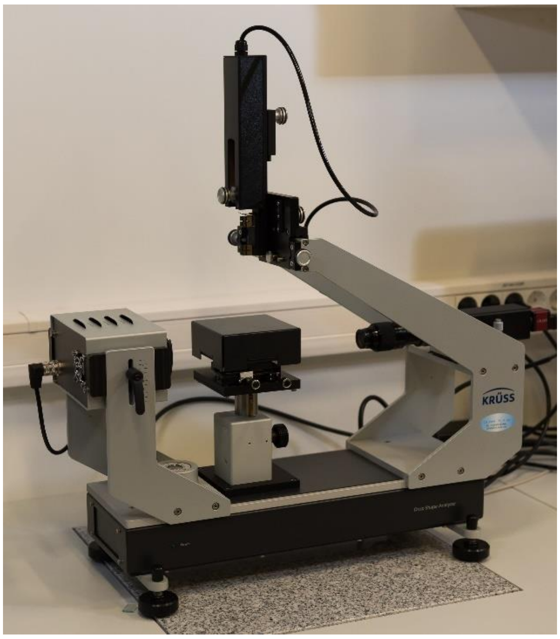

Figure 16. Contact angle measurement device DSA25 (Kruss) [40].

3. Results

3.1. Failure Analysis

Since this work was a continuation of my bachelor's degree thesis [41], several samples were devoted to analysis of how to improve the procedures and reduce the number of failed samples. One of such failures was caused by "comets" in the photoresist seen in Fig. 17. Samples F21 and F22 were made in a slightly different way, *i.e.*, after coating with a photoresist and heating on a heat plate, they were not cooled down with nitrogen gas, but instead after cooling down for a few seconds in the air were placed on a Petri dish. However only part of these samples had areas with no comets. Another sample F23 was made with a regular procedure but was heated for 6 minutes after it was exposed to UV light. Once again only a small area had no comets, indicating that heating or no heating had little effect on the formation of these comets. Samples whose name starts with G, such as G2 and G3, were fabricated with fresh silicon substrates, and only one from these samples had "comets" on them, which were accompanied by dust at the place where the comet begins. Since the new silicon sample was clean, the resulting particles appeared most likely during and after the development step. And since the dust particles did not disappear after blowing with nitrogen gas, one reason for the comets may be that blowing by nitrogen gas is done with a too high flow rate. The sample in Fig. 17 shows that all the comets are facing from the center of the sample, where the nitrogen gas is blown to. Therefore, the most likely reason for such unwanted structures was dust particles stuck on the sample, being blown with a too high flow of nitrogen gas, causing the area around and behind the particles to experience an increased flow of gas and removing some photoresist from those areas. This is also evidenced by the comet area appearing similar to the parts of the sample with no photoresist left, Fig. 17 bottom right. Due to this, the comets may be avoided by using a lower nitrogen gas flow and changing the angle at which the nitrogen is blown on the samples during the drying step after developing the sample.

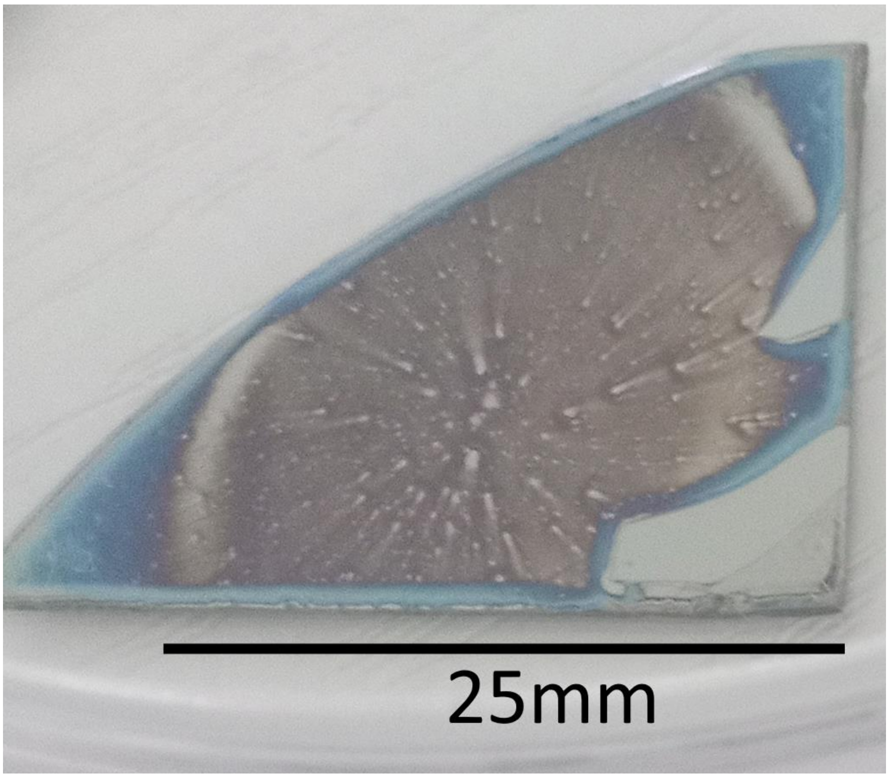

Figure 17. Camera image of the "comet" like structures on sample G1.

Afterward samples F24 and F25 were made to have a superlattice of 20 µm and pitch made from 299.6 nm and 295.50 nm, however, the usual amount accumulated energy dose of 30 mJ/cm^2 appeared to be too much, even though the development time was the same, 10 seconds. The power during the exposure was higher than usual, but that was already accounted for when calculating the required exposure duration. The photoresist structures only remained on the sample, when the exposure energy was less than 20 mJ/cm^2. Such a massive difference is difficult to find an explanation for, however, this had happened a few times before, during bachelor's final degree projects [41]. One of the reasons could be related to higher humidity. Unfortunately, due to this happening rarely, it was not studied extensively.

3.2. Water contact angle measurements

Since hierarchical structures were able to achieve super hydrophobicity in [30], dedicated superlattices were made to check their contact angle dependence on the superlattice pitch. Sample F27 was patterned to have pitch of 299.96 nm, and was divided into four parts, and each exposed another time with a different period and had different superlattice period of: F27.1 298.20 nm nanostructure and 50 µm superlattice; F27.2 299.10 nm nanostructure and 100 µm superlattice; F27.3 299.95 nm nanostructure and 200 µm superlattice; F27.4 299.91 nm nanostructure and 1000 µm superlattice. The resulting contact angles of structures in the photoresist are seen in Fig. 18. The angles were below 40°, even though the contact angle with the unexposed photoresist was 70^o. There were some deviations in the angle value since the samples were measured within a few minutes after developing and drying with nitrogen gas, it was suspected that there may have been some water or developer left on the sample. Therefore, more samples were made to analyze the effects of nanostructure, water, developer, and heating on the contact angle. Sample F28 was made with a simple 599.97 nm structure, using 30 mJ/cm^2 dose. Sample F29 was held in the laser beam, before the sample holder and mirror system, causing a homogeneous exposure without nanostructures. Sample F30 was not exposed to light in any way and was used as a reference for the photoresist. The contact angles were measured after developing the sample, heating the sample, submerging the sample in water, and reheating it again. The resulting contact angles are shown in Fig. 19. Initially, all three samples showed similar contact angles, with the nanostructured one having a slightly higher contact angle. After the water was blown away from the samples using compressed air, they were placed on a hotplate with a temperature of 85^o for 5 minutes and were measured again. The contact angle increased by several degrees in each case. Afterward the samples were immersed in type 2 deionized water for 30 seconds. Then they were dried with compressed air, and contact angles were measured again. The sample with no exposure to UV had a lower contact angle than initially, the sample that was exposed homogeneously by UV light returned to the initial angle, and the contact angle of the nanostructured sample increased higher than after heating. After reheating all the samples, the not exposed sample returned to the initial contact angle, the homogeneously exposed sample had a significantly increased contact angle, and the nanostructured sample had the highest contact angle. While the unexposed sample behaved as expected, the nanostructured and homogeneously exposed samples had increased contact angles even after they were submerged in water. One explanation for this may be that not all of the exposed areas were developed away, or there might have still been some developer left on the samples, which was then removed after stirring in water.

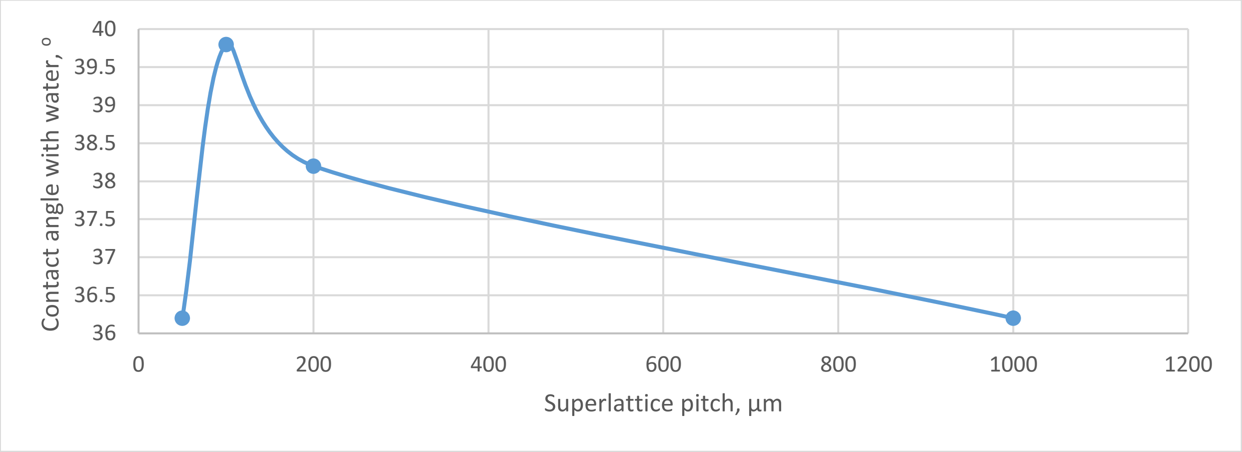

Figure 18. Contact angle with water dependence on superlattice pitch.

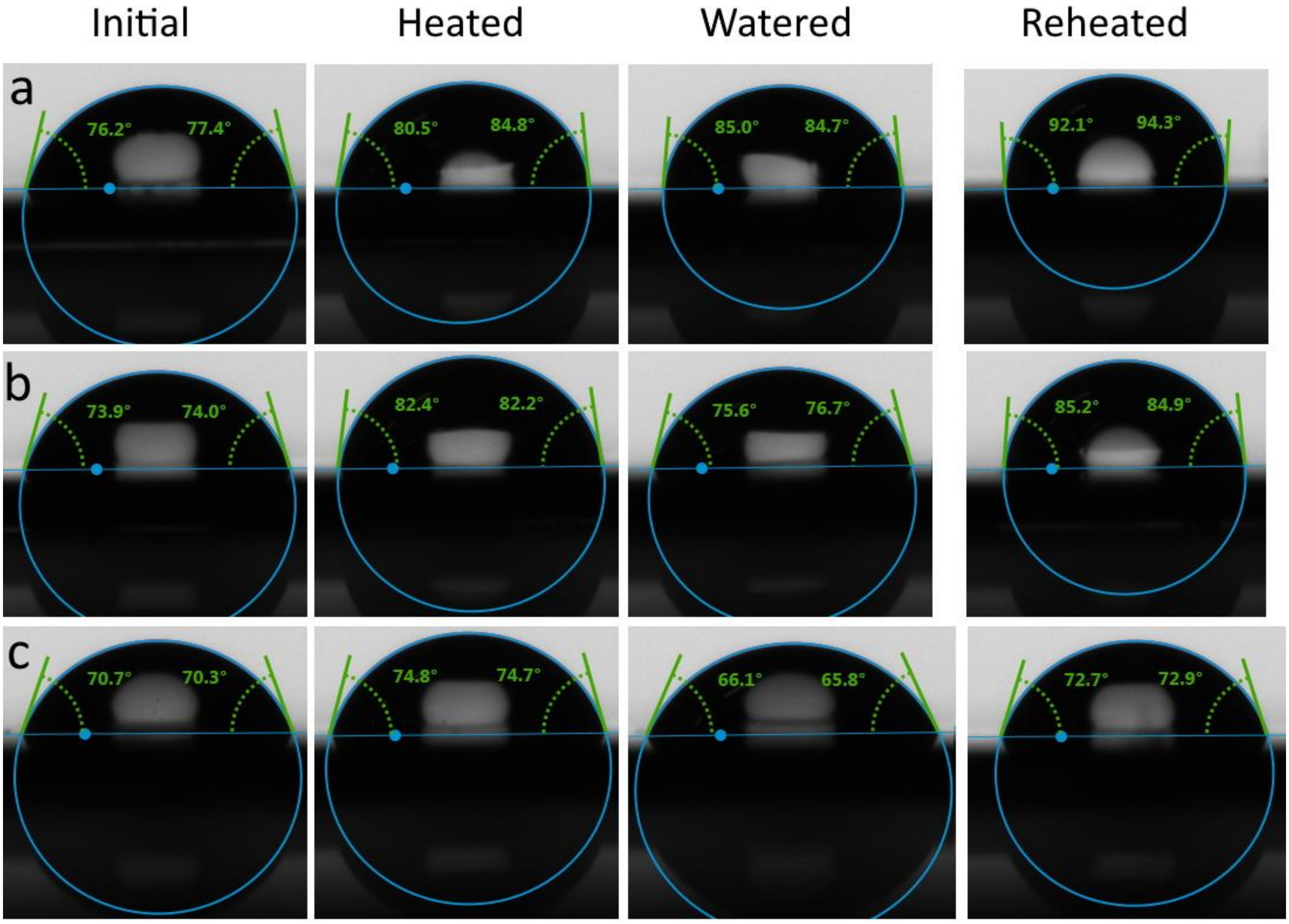

Figure 19. Contact angles of sample (a) F28 that has regular 600 nm grating, (b) F29 that was placed into a single beam of light, and (c) F30 that was placed in developer, without any exposition to laser light.

Afterward samples F31, F32, F33, F34, F35, F36, F37 were made with 10 µm superlattice structures and nanostructures of: F31 299.96 nm and 291.02 nm; F32 299.96 nm and 291.02 nm, F33 200.00 nm and 196.00 nm; F34 200.00 nm and 196.00 nm; F35 200.00 nm and 196.00 nm; F36 200.00 nm and 196.00 nm; F37 200.00 nm and 196.00 nm, and their contact angles were measured, with them being rinsed in water for longer, to remove any developer solution leftover. Samples F33 and F34 received much higher exposure energy based on previous experience of working with thicker resist layers

(500 nm) where higher doses were required for smaller pitches. However, for 100 nm photoresist, the energy dose was too high. Afterward, each sample was measured at 2 spots, and the resulting contact angles are shown in Fig. 20. The samples that were exposed too much, F33, F34 and F37 (marked in red), showed a contact angle, similar to that of unexposed photoresist after submersion in water, and were placed at 0nm nanostructure period point in the graph. Samples F31 and F32, which had a structure pitch of 299.96 nm and 291.02 nm, had a much lower contact angle than 599.97 nm grating structure of F29, with the angles being between 48° and 57°. When the structure pitches were 200.00 nm and 196.00 nm, in sample F35, the contact angle was between 43° and 49°, which was even lower than F31 and F32. The large contact angle difference at 200.00 nm and 196.00 nm nanostructure period is because the one of the samples they were measured on, F36 marked in red at 200nm mark, was inhomogeneous, with patches of completely developed away photoresist, and that may have caused the measured angle to be closer to that of samples F33, F34 and F37, which had all photoresist developed away.

This seems to indicate that lowering the structure pitch would decrease the contact angle, however, there are not enough samples to conclude. Since in [30], the structures were additionally coated with fluorine compounds, which significantly reduce surface tension, and without them, the results between contact angles of different structures are not very high.

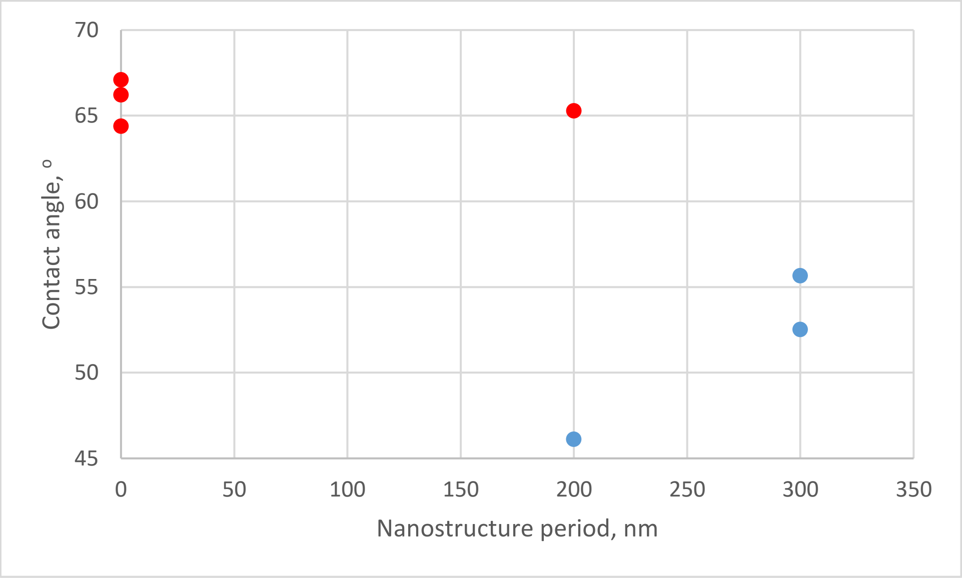

Figure 20. Water contact angle with dependence on nanostructure period, while superlattice period remains 10 µm. 0 nm nanostructure period represent overexposed sample with no photoresist left after development. Data from samples F31, F32, F33, F34, F35, F36, F37.

3.3. Analysis of Superlattices

Sample F38 was done by making a 599.97 nm and 599.80 nm nanostructures with a superlattice of 1.1 mm in one direction, and then 250.01 nm and 249.97 nm nanostructures and superlattice of 1.6 mm in a perpendicular direction. However, the sample was unevenly coated with photoresist, and only a few patches were left after the development of the sample, and exposure was insufficient since, on the few patches of photoresist left, it needed over a minute of developing, for diffraction to appear from the sample. Afterward samples F39 and F40 were made to check if there are at least a few millimeters of intersecting areas, when a sample is rotated by 60° and -60°, however, no area intersected. Then a beam-expanding optical element (concave lens) was added after the spatial filter, and the beam expanded several times, but the power density measured at the center of the sample holder and mirror decreased from 130 µW/cm^2 to 21 µW/cm^2. Then samples F41, F42, F43, and F44 were made by rotating the sample either 60° or 30° to check if the exposure now correctly covers the entire area. The structures were confirmed, by the millimeter-sized superlattices, since pitches lower than 400 nm are impossible to see with an optical microscope and checking samples daily with an electron microscope would take an extraordinary amount of time. Structures with pitches higher than 300 nm were not able to utilize the vertical rotation of the sample holder, since the reflection from the mirror was too small to reach the center of the vacuum holder, due to the physical size of the mirror.

Samples were made and their superlattices were measured (see Fig. 21) with these parameters: (a) F45 998.10 nm and 998.18 nm, (b) F46 500.16 nm and 499.94 nm; (c) F47 249.97 nm and 249.93 nm; (d) F49 200.00 nm and 196.00 nm. These parameters were chosen so that the superlattices were on the order of a millimeter, to see if the superlattices are visible with the selected pitches. The superlattices are shown in Fig. 21. Sample F48 did not receive enough exposure, and nothing was visible on the surface after developing for a minute, therefore results are not displayed. A caliper was used to measure a screw, with a resolution of 0.1 mm, and that was used as a reference size for superlattice period calculation. The experimental values were acquired by measuring however many lines that were the most visible, and then the number of superlattice periods was divided by measured distance. In all of the samples, the superlattice lines were clearly visible, even when the nanostructure pitch was lower than 250nm, at which point the diffraction of the sample is only visible at nearly 90° angle from sample surface. In Fig. 21 d, the measured experimental period is 1mm, which means that the height variation of the photoresist layer of 100 nm per millimeter is clearly distinguishable. The experimental values are within 10% of the theoretical values. If the samples were larger or had lines that were more defined, more lines could have been measured, and the error could be reduced.

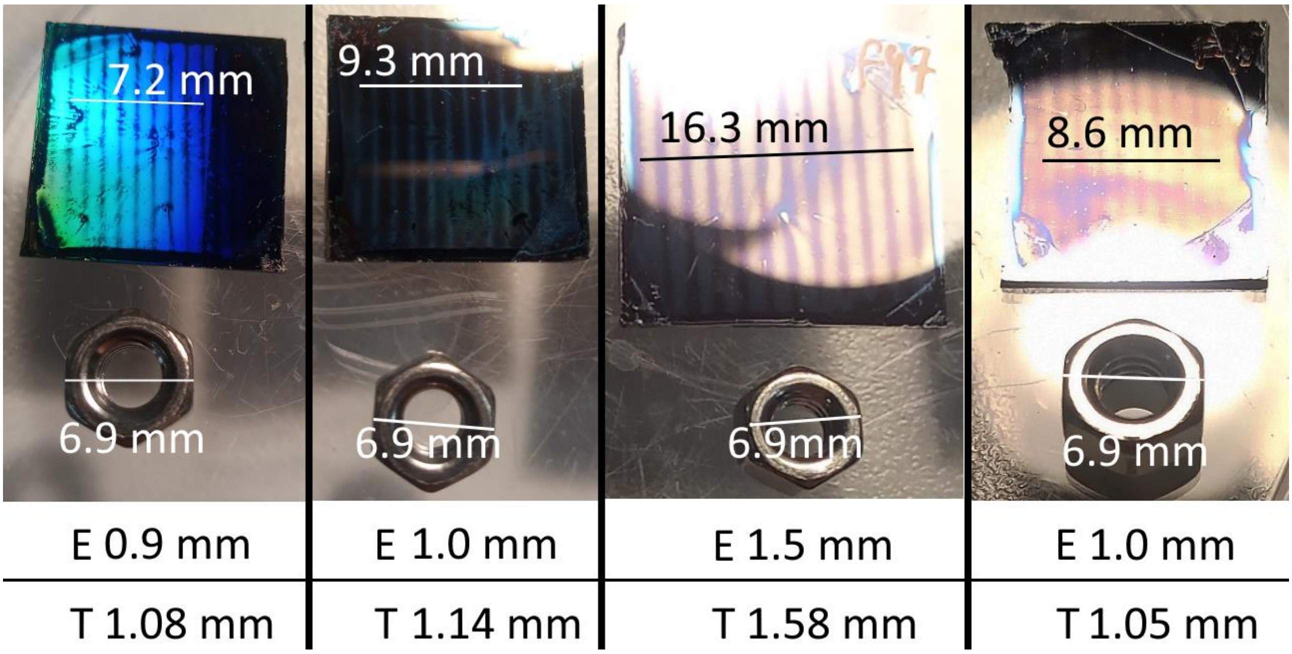

Figure 21. Superlattices and their nanostructures: (a) sample F45 998.10 nm and 998.18 nm, (b) F46 500.16 nm and 499.94 nm; (c) F47 249.97 nm and 249.93 nm; (d) F49 200.00 nm and 196.00 nm. A nut is placed for scale, which was measured with a caliper. The error in measurements was ±0.1 mm. The measured values have E written next to them, while theoretical values have T.

Sample G2 was done with a fresh silicon substrate, to see whether it would have as many defects, as the cleaned and reused silicon. The structures were exposed as a superposition of 599.97 nm, 592.66 nm, 585.53 nm pitches in one direction and again at 90^{o} rotation. The resulting structure is shown in Fig. 22. The theoretical superlattice pitch is 50 µm, while the measured nanostructure pitch is 520 nm.

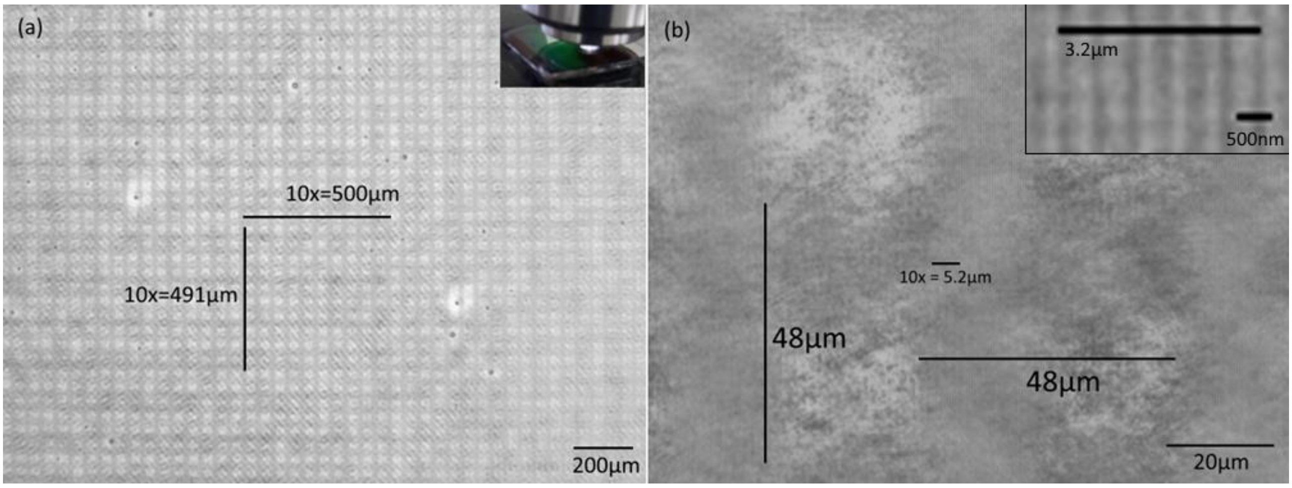

Figure 22. Optical microscope images of sample G2. (a) 75X magnification image. (b) 1500X magnification image. The inset of (b) shows a sample diffracting green light under white light illumination from the microscope.

Although each exposure added a sinusoidal variation, the optical microscope images show that the superlattice patterns are more rectangular than circular.

The accumulated light intensity distributions analogous to experimental ones were explored theoretically using simulations in MATLAB. From the theoretical results (Fig. 23 a, b) it can be seen that two sinusoidal exposures cause the spatial light distribution containing circle-like shapes, while three exposures caused a clover-like shape. The 3D representations of the accumulated intensity distributions (Fig. 23 c, d) even more clearly show that the squares are less exposed areas, and they are separated by several circular structures, which causes the clover shape seen in Fig. 19 (b). In Fig. 22 (a) a large number of superlattice structures are seen, and they have some defects, which appear as some parts of the squares missing. The cause for this type of defect was not found but may be due to the developing being done manually by hand, instead of an automated process.

Since the code in MATLAB allows not only several different periods of structures and rotations but also enables changing the intensity of each exposure, some simulations were done to explore the effect of non-equal exposure durations. Fig. 24 (a) shows regular circular structures in a square arrangement obtained after two exposures of 600.00nm and 592.80nm period, and repeated exposures with 90° sample rotation. In Fig. 24 (b), additional exposure with a period of 237.50 nm and 1/3 the exposure duration in 0^{o} and 90^{o} rotations, shows that the circular peaks become reduced from the corners, causing the valleys to become larger, and squarer. Fig. 24 (c) shows that if all exposures are equal, the holes become very much square-like, and the sides of the holes have additional periodic variation. An important thing to note is that the positions of the superlattice peaks are the same in all three cases. By understanding this, one can choose additional exposure with such period and exposure duration, that the shape of the holes changes, while the shape of the hole walls, does not change as much, while all peaks are in the same positions.

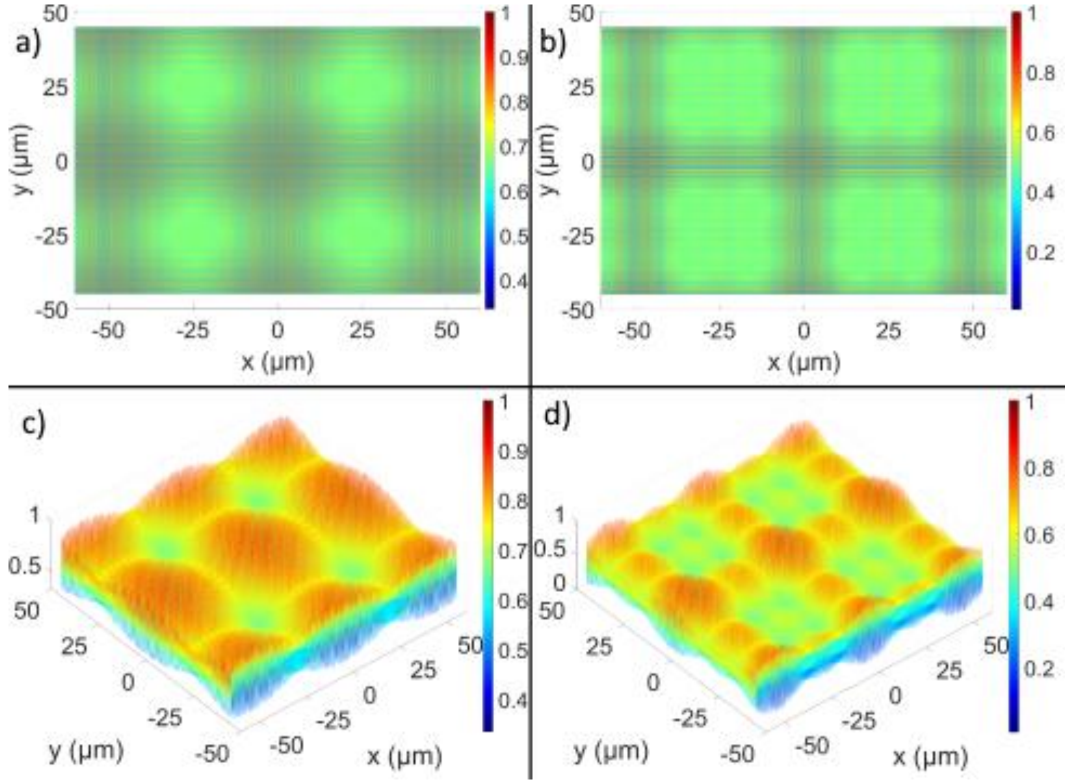

Figure 23. Spatial light intensity distributions simulated with MATLAB. (a) top view simulation of 600 nm+592.8 nm structure. (b) top view simulation of 600nm+592.8nm+585.6nm structure (sample G2). (c) 3d side view simulation of a). (d) 3d side view simulation of b).

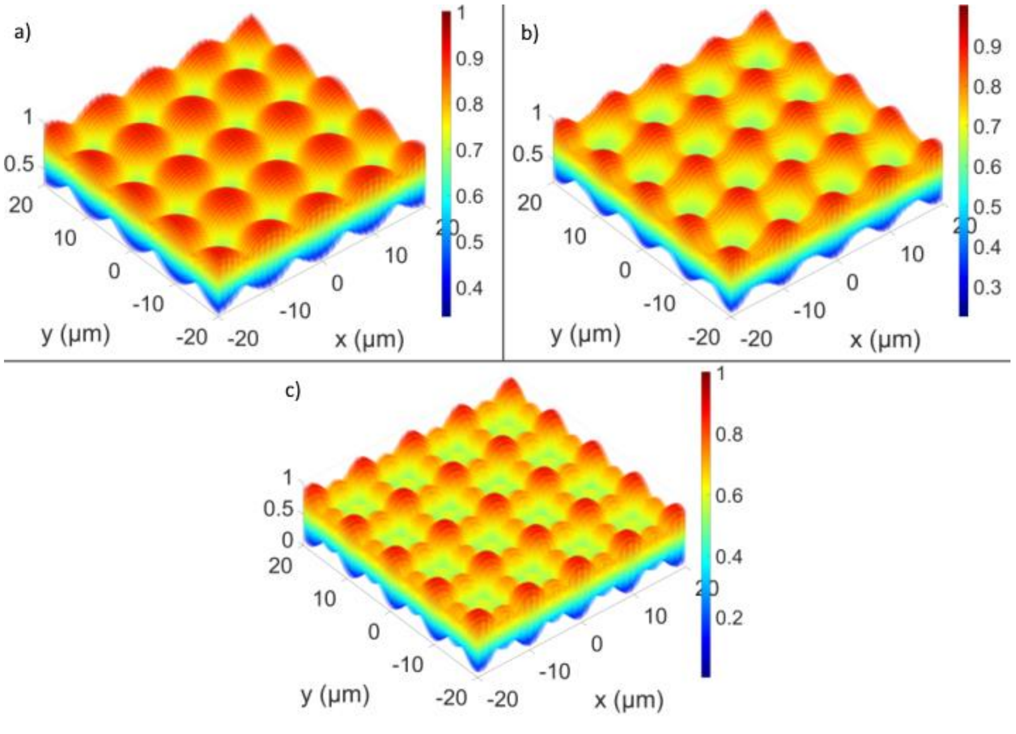

Figure 24. MATLAB 3D side view images of simulations of different durations for exposures. (a) 250 nm+243.75 nm of equal exposure duration superlattice. (b) 250 nm+243.75 nm equal duration exposures + 237.5nm exposure at 1/3 the duration of other exposures. (c) 250 nm+243.75 nm+237.5 nm equal duration exposures.

3.4. Hexagonal Superlattices

Samples G4 and G5 were done to further explore the effect of the third exposure on a superlattice, in this case, a hexagonal superlattice was investigated. Sample G4 was done with 599.97 nm and 592.66 nm exposures at -60^{o}, 0^{o}, 60^{o} rotations. Sample G5 was done with 599.97 nm and 592.66 nm and 585.53 nm exposures at -60^{o}, 0^{o}, 60^{o} rotations.

Fig. 25 shows optical microscope images of sample G4, in an area reached by all the exposures. The superlattice period should be 48µm, while the measured value was 50µm (see Fig. 25 a). The hexagonal pattern similar to the simulation, Fig. 26 (a), can be seen in the 1500x magnification image of Fig. 25 (b). Interestingly the optical microscope image shows a lot of closely packed squares, which are further magnified in Fig. 25 (c). The simulation of this sample does not show such squares, however due to time constraints, a detailed analysis of the origin of the squares on the sample has not been carried out.

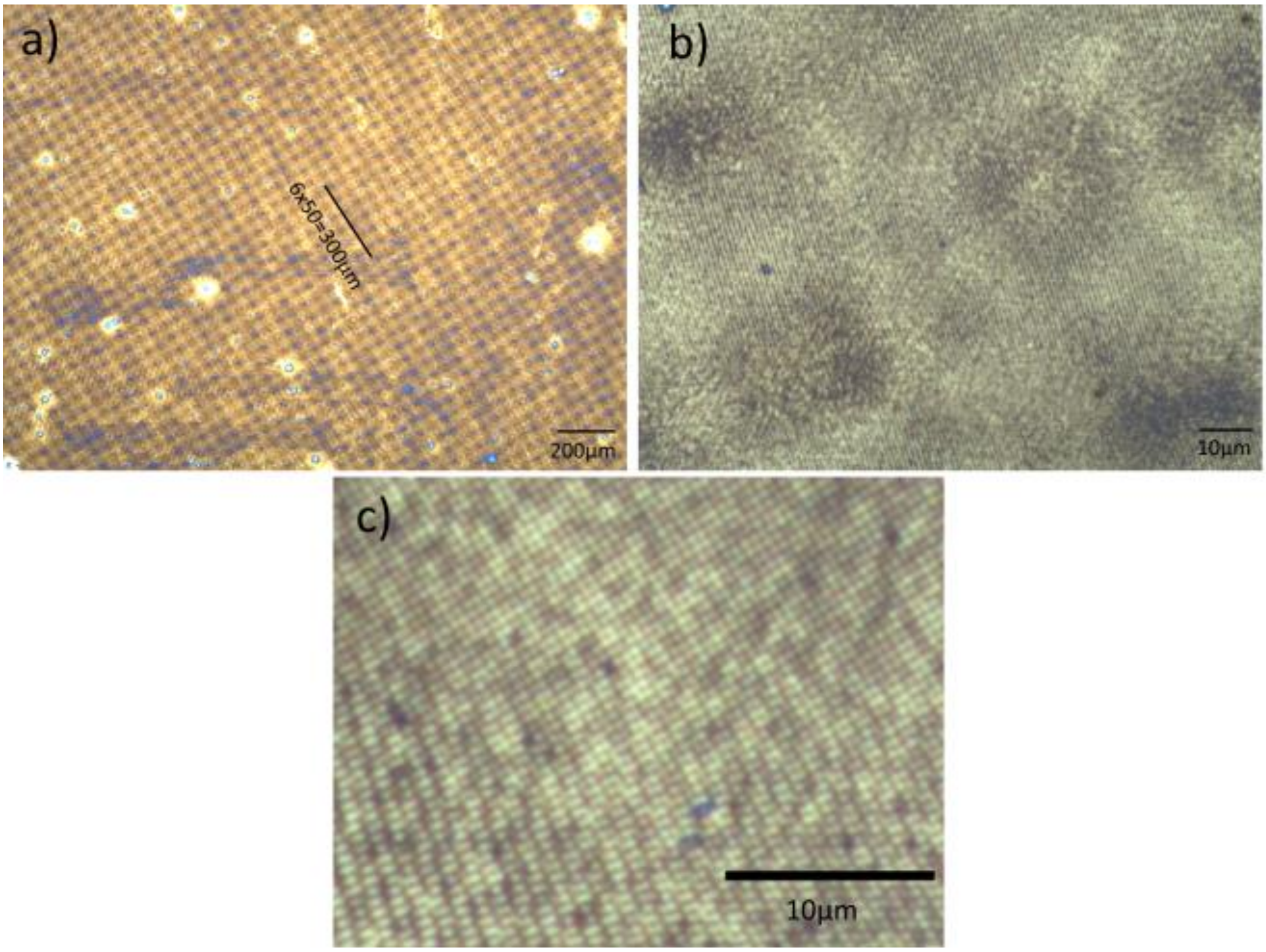

Figure 25. Optical images of sample G4. While in 75x magnification (a) the structure seems like an array of squares, at 1500x magnification (b) the hexagonal pattern is easily visible. (c) shows square nanostructures which are not present in simulated images.

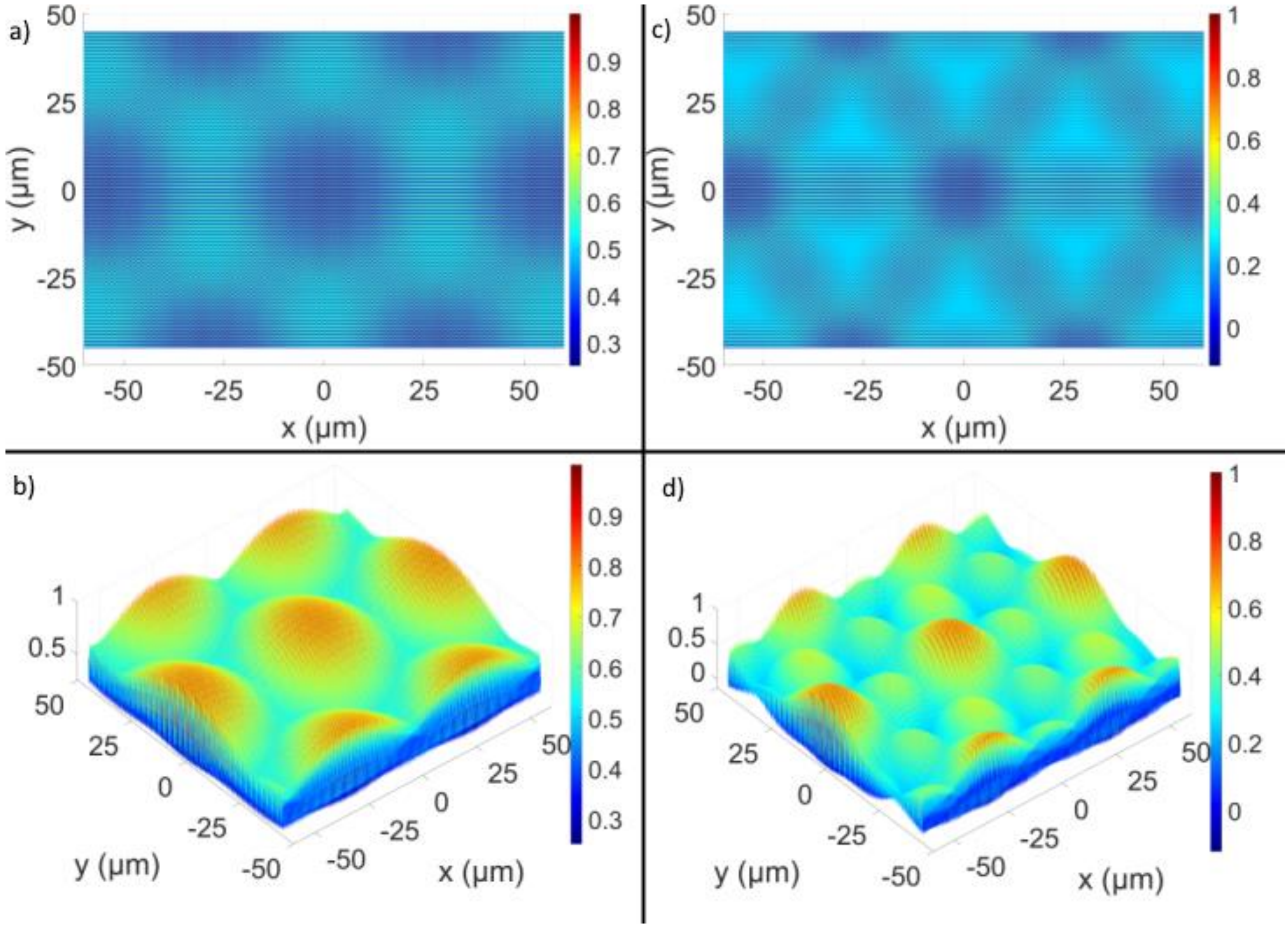

Figure 26. MATLAB simulations of hexagonal superlattices. (a) and (b), top and side view respectively of 600 nm+592.8 nm hexagonal superlattice G4. (c) and (d), top and side view respectively of 600 nm+592.8 nm+585.6 nm hexagonal superlattice G5.

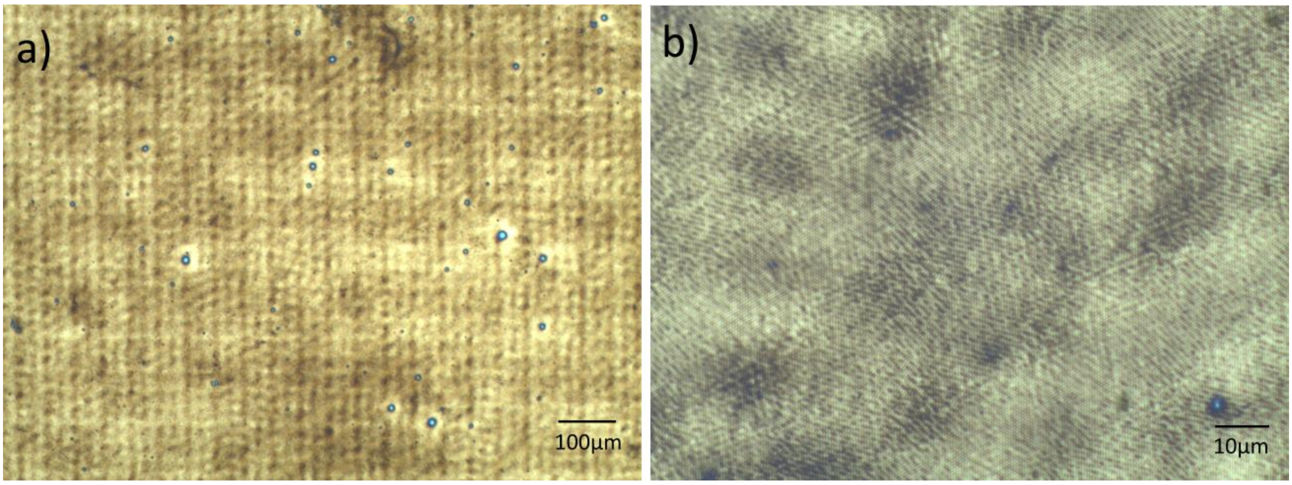

Figure 27. Optical images of sample G5 at (a) 150x magnification and (b) 1500x magnification.

Sample G5 at 1500x magnification, Fig. 27 (b) looks slightly similar to the simulation, Fig. 26(c), however, the superlattice structure seems deformed. The cause of these deformations is not known, but it could be caused by the sample slipping from the sample holder, since it was placed off-center, and had to be manually rotated by 60°. Even with these deformations, there is a clear difference between samples G4 and G5, since in G4, the superlattice structure is larger in size, while sample G5 looks patterned with smaller superlattice structures Fig. 27(b).

Sample G6 was done to check the minimal vertical rotation of the sample holder, which was 0.13°. The resulting Moiré structure was clearly visible with the naked eye, however, a camera image of the sample was not made. Another sample done was G8, which was made to have superlattices of around 1.5 mm, and was rotated by 36° vertically 4 times, with a total number of exposures being 10, and the energy for each separate exposure being 3.2 mJ/cm^2. However, this proved to be too much, and no photoresist was left after the usual development procedure. Therefore, sample G9 was done with the same parameters, but energy of 2.9mJ/cm^2 for each exposure. The nanostructures were smaller than 250 nm, therefore the optical microscope could not show the nanostructures. A simulation of the sample structure is shown in Fig. 28(a)m and camera image of the sample in white light is shown in Fig. 28 (b), where the superlattice structure is visible, even though the height variation over the sample is less than 100 nm. Unfortunately, since the sample was not done in a clean room, there is contamination present on the sample.

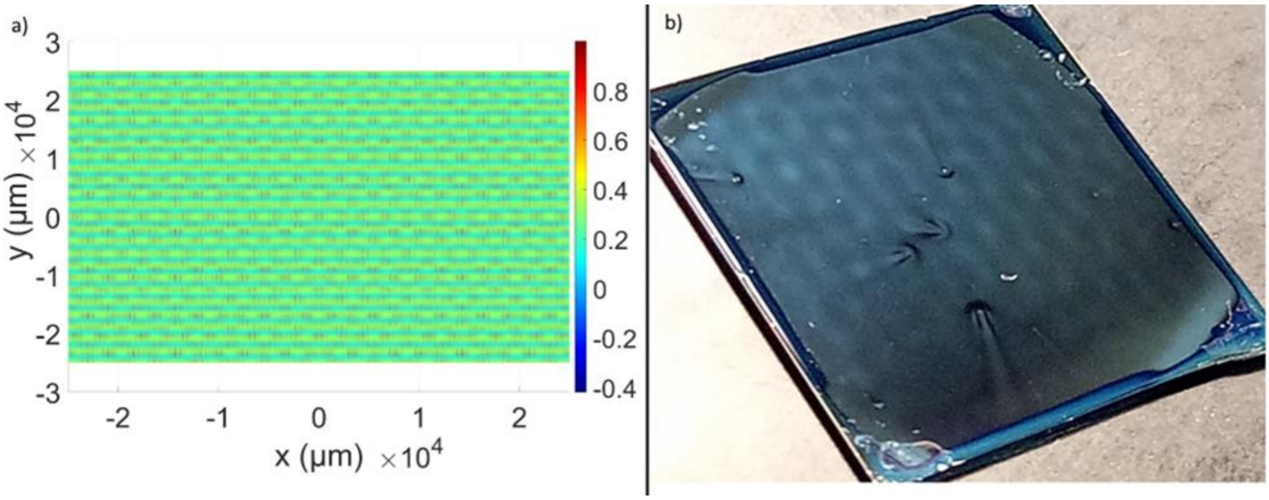

Figure 28. Sample G9. (a) simulation results, (b) camera photo. The sides of the silicon piece are 25 mm x 25 mm.

Participation in conferences

Parts of this work were presented in a conference for students, hosted by Student Union FUMSA and the Mathematics and natural sciences faculty of Kaunas University of Technology, “Matematika ir gamtos mokslai: teorija ir taikymas” with the topic “Moiré and superlattice fabrication using holographic lithography” (oral presentation).

Conclusions

1. Superlattice structures with periods over 1 mm and nanostructure periods of 999 nm, 500 nm, 250 nm, 200 nm, were fabricated in positive tone photoresist over cm^2 scale areas using holographic lithography.

2. A height variation less than 100 nm over the distance of a millimeter is clearly detectable by the human eye.

3. By using 3 exposures of 250.01 nm; 243.75 nm; and 237.49 nm periods and modifying the dose of the third exposure to a third of the other doses, one can change the size and shapes of periodic elements, causing them to be squarer, while not forming significant additional superlattice structures and leaving the superlattice period the same.

4. A code was written in MATLAB software, which allows to simulate any number of exposures where exposure energy, interference period, angle tilt, simulation area and resolution can be freely chosen. This was used in optimizing the exposure energy for changing the shape of superlattice peaks, while retaining the same superlattice period. This code produces reliable results when the photoresist thickness is 100 nm.

5. The appearance of unwanted comet-like structures on the samples can be minimized, by reducing the flow of gas, during the drying step of the photoresist development.

6. Preliminary results show that 10 µm superlattice structures covered with 200 nm nanostructures have a lower contact angle with water, than the same period superlattice structures with 300 nm nanostructures.

List of References

[1] “*Lithography*.” [online]. [Accessed 9 May 2022]. Available from: https://www.merriam-webster.com/dictionary/lithography

[2] Micronit. *Lithography processes by Micronit: photolithogrtaphy and nano-imprint*. [online]. [Accessed 2022 May 09]. Available from https://www.micronit.com/manufacturing/capabilities/lithography

[3] ASML “*Technology Strategy – martin van den Brink*” [online]. [Accessed 9 May 2022]. Available from https://www.asml.com/en/investors/investor-days/2021

[4] CNBC “*Inside ASML, the company advanced chipmakers use for EUV lithgraphy*”. [online]. [Accessed 9 May 2022]. Available from https://www.cnbc.com/2022/03/23/inside-asml-the-company-advanced-chipmakers-use-for-euv-lithography.html

[5] HENK van Wolferen and Leon Abelmann *„Laser Interference lithography*“ Lithography: Principles, Processes and Materials. Nova science Publishers 2011. ISBN:978-1-61761-837-6

[6] Wikipedia “Moire (pattern)” [online]. [Accessed 9 May 2022]. Available from https://en.wikipedia.org/wiki/Moir%C3%A9_pattern

[7] RUSSEL et all. “*Creating Two-Dimensional Quasicrystal, Supercell, and Moiré Lattices with Laser Interference Lithography: Implications for Photonic Bandgap Materials*” ACS Appl. Nano Mater. 2021, 4, 8851−8862

[8] BALCI, S., Karabiyik, M., Kocabas, A., Kocabas, C., & Aydinli, A. (2010). “*Coupled Plasmonic Cavities on Moire Surfaces”*. Plasmonics, 5(4), 429–436. doi:10.1007/s11468-010-9161-8

[9] Gómez-Urrea, H.A.; Ospina-Medina, M.C.; Correa-Abad, J.D.; Mora-Ramos, M.E.; Caro-Lopera, F.J. (2019). *“Tunable band structure in 2D Bravais-Moiré photonic crystal lattices*”. Optics Communications, (), 125081–. doi:10.1016/j.optcom.2019.125081

[10] JOANNOPOULOS, J. D., Villeneuve, P. R., & Fan, S. (1997). „*Photonic crystals: putting a new twist on light*“. Nature, 387(6635), 830–830. doi:10.1038/42999

[11] USHKOV et all., „*Subwavelength diffraction gratings with macroscopic moiré patterns generated via laser interference lithography*“ Vol. 28, No. 11 / 25 May 2020 / Optics Express https://doi.org/10.1364/OE.386699

[12] MicroChemicals “*COMPOSITION AND PROPERTIES OF AZ® AND TI PHOTORESISTS*“ [online]. [Accessed2 4 April 2022]. Available from https://www.microchemicals.com/technical_information/photoresists_composition_properties.pdf

[13] MicroChemicals „*Spin-Coating*“[online]. [Accessed 4 May 2022] Available from https://www.microchemicals.com/technical_information/spin_coating_photoresist.pdf

[14] Microresist technology „*mr-P 1200LIL series*“[online]. [Accessed 4 May 2022]. Available from https://www.microresist.de/en/produkt/ma-p-1200-lil-series/

[15] MicroChemicals “*Lithography Trouble Shooter Questions and Answers Around the Most Common Problems in Micro- Structuring*”. [online]. [Accessed 10 May 2022] Available from https://www.microchemicals.com/technical_information/TroubleShooter_EN.pdf

[16] ASML Technology „*Supplying the semiconductor industry*“. [online]. [Accessed 4 May 2022]. Available from https://www.asml.com/en/technology

[17] Intel „*EUV: the most precise, complex machine at Intel*“. [online]. [Accessed 4 May 2022] Available from https://www.intel.com/content/www/us/en/newsroom/news/euv-most-precise-complex-machine.html#gs.zez5xm

[18] PALMER, Christopher. *DIFFRACTION GRATING 8th edition*. MKS Instruments Inc.

[19] SHAHIN Bagheri, et al., “*Large-Area Low-Cost Plasmonic Perfect Absorber Chemical Sensor Fabricated by Laser Interference Lithography*” ACS Sens. 2016, 1, 9, 1148-1154. Publication Date: August 24, 2016

[20] C. -C. Lin, J. -S. Chen, C. -L. Wu, L. A. Wang and N. -T. Huang, "*A Nanodisk Array Based Localized Surface Plasmon Resonance (LSPR) Sensor Fabricated by Laser Interference Lithography,*" 2019 IEEE 14th International Conference on Nano/Micro Engineered and Molecular Systems (NEMS), 2019, pp. 217-220, doi: 10.1109/NEMS.2019.8915617.

[21] ERTUGRUL Karademir et all. „*Lasing in a Slow Plasmon Moiré Cavity*“ ACS Photonics 2015 2 (7), 805-809 DOI: 10.1021/acsphotonics.5b0016

[22] USHKOV et all., „*Systematic study of resonant transmission effects in visible band using variable depth gratings*“ Scientific Reports | (2019) 9:14890 | https://doi.org/10.1038/s41598-019-51414-3

[23] Langer et all. „*Present and Future of Surface-Enhanced Raman Scattering*“ ACS Nano 2020, 14, 1, 28–117 Publication Date: September 3, 2019 https://pubs.acs.org/doi/10.1021/acsnano.9b04224

[24] Seong Jae Kim et al 2021 „*Exploring SERS from complex patterns fabricated by multi-exposure laser interference lithography*“ Nanotechnology 32 315303

[25] Mehrvar, L., Sadeghipari, M., Tavassoli, S.H. et al. “*Optical and Surface Enhanced Raman Scattering properties of Ag modified silicon double nanocone array*”. Sci Rep 7, 12106 (2017). https://doi.org/10.1038/s41598-017-12423-2

[26] Kloubek, J. (1992). “*Development of methods for surface free energy determination using contact angles of liquids on solids”*. Advances in Colloid and Interface Science, 38, 99–142. doi:10.1016/0001-8686(92)80044-x

[27] Huhtamäki, T., Tian, X., Korhonen, J. T., & Ras, R. H. A. (2018). “*Surface-wetting characterization using contact-angle measurements*”. Nature Protocols, 13(7), 1521–1538. doi:10.1038/s41596-018-0003-z

[28] Fadda, E. (1995). “*Characterization of latent image by surface energy determined by contact angle measurements*”. Journal of Vacuum Science & Technology B: Microelectronics and Nanometer Structures, 13(3), 1055. doi:10.1116/1.587902

[29] Latthe, S., Terashima, C., Nakata, K., & Fujishima, A. (2014). “*Superhydrophobic Surfaces Developed by Mimicking Hierarchical Surface Morphology of Lotus Leaf. Molecules*”, 19(4), 4256–4283. doi:10.3390/molecules19044256

[30] Han, J. et all. “*Comprehensively durable superhydrophobic metallic hierarchical surfaces via tunable micro-cone design to protect functional nanostructures*”. RSC Advances, 2018(12), 6733–6744. doi:10.1039/c7ra13496g

[31] Ma, M., & Hill, R. M. (2006). “*Superhydrophobic surfaces*”. Current Opinion in Colloid & Interface Science, 11(4), 193–202. doi:10.1016/j.cocis.2006.06.002

[32] Roach, P., Shirtcliffe, N. J., & Newton, M. I. (2008). “*Progess in superhydrophobic surface development*”. Soft Matter, 4(2), 224–240. doi:10.1039/b712575p

[33] CrystaLaser, „*Stabilized Violet-blue 375/ 405/380 to 488nm Lasers*“. [online]. [Accessed 19 May 2022] Available from http://www.crystalaser.com/DL375-488.pdf

[34] Standa Opto-Mechanical Products, „*10SF130 - Precision Spatial Filter*“. [online]. [Accessed 19 May 2022] Available from www.standa.lt/products/catalog/opto_mechanics?item=125&prod=precision_spatial_filter

[35] Newport mks „*U-27X-LC*“. [online]. [Accessed 19 May 2022] Available from https://www.newport.com/p/U-27X-LC

[36] Standa "*Motorized Rotation Stages - Motorized Positioners & Controllers - Catalog - Opto-Mechanical Products – Standa*. [online]. [Accessed 17 May 2022]. Available from https://www.standa.lt/products/catalog/motorised_positioners?item=9&prod=motorized_rotation_stages

[37] "*Optinis mikroskopas su fluorescencijos* priedu". [Accessed 21 May 2022]. Available from https://apcis.ktu.edu/MMI/lt/site/katalogas?cat_id=115&more=6724&type=1

[39] "*Fiji*". [Accessed 21 May 2022]. Available from https://imagej.net/software/fiji/

[38] EBNESAJJAD, Sina and EBNESAJJAD, Cyrus F. "*Surface treatment of materials for adhesive bonding*". . Second edition 2014 ISBN 978-0-323-26435-8 TA418.7 .E24 2014

[40] "*Vilgumo kampo matuoklis Kruss, Drop Shape Analysis System DSA25*". [Accessed 21 May 2022]. Available from https://apcis.ktu.edu/MMI/lt/site/katalogas?cat_id=115&more=9117&type=1

[41] Klyvis Gvidas, "2D Nanostructures for Optical Sensors", Bachelors thesis, Kaunas university of technology 2020